Protection of Transmission Lines Connected to IG-Based Wind Farms

by

Javad Zare

A thesis
presented to the University of Waterloo
in fulfillment of the
thesis requirement for the degree of
Master of Applied Science
in
Electrical and Computer Engineering

Waterloo, Ontario, Canada, 2020

Author's Declaration

I hereby declare that I am the sole author of this thesis. This is a true copy of the thesis, including any required final revisions, as accepted by my examiners.

I understand that my thesis may be made electronically available to the public.

Abstract

Over the last few decades, renewable energy sources have been attracting great attention due to the increased cost, limited reserves, and the adverse environmental impact of fossil fuels. Among them, wind energy is one of the fastest-growing renewable energy sources worldwide. Wind farms (WFs) comprise a considerable share of the installed capacity of renewable sources in the power grids. With the large integration of WFs in the power grid, the fault ride-through (FRT) requirement has become an essential part of the modern grid codes to increase grid reliability and stability. WFs with FRT capability are required to remain connected to the power grid during fault conditions for a specific period. This will result in WFs contributing to the fault current and changing the system fault current characteristics. Such changes in the fault current characteristics significantly affect the operation of the protection systems.

This dissertation will mainly focus on doubly fed induction generator (DFIG)-based WFs and will study their negative impacts on the operation of conventional protection relays, particularly the ones that protect the transmission lines connected to DFIG-based WFs. Considering different negative impacts of DFIG-based WFs on protection systems due to their large slip range, the short-circuit behaviour of a DFIG is evaluated in two different aspects: 1) close-to-zero slip operation and 2) large slip operation. During close-to-zero slip operation of a DFIG-based WF, the short-circuit behaviour of the DFIG is similar to that of a fixed-speed squirrel cage induction generator (SCIG); therefore, fixed-speed SCIG-based WFs are also evaluated in this dissertation. In this situation, a conventional distance relay located at the fixed-speed SCIG or DFIG terminal fails to operate correctly and loses its coordination with the downstream relays for a balanced fault in its backup zone due to the negligible magnitude of the fundamental component of the fault current after several hundred milliseconds. Regarding DFIG-based WFs with FRT capability during large slip operation, the fault current frequency fed by DFIG-based WFs deviates from the nominal frequency during a fault, which affects the operation of conventional protection relays with distance or frequency elements.

In this dissertation, two new relaying schemes based on distance elements for the protection of transmission lines connected to the fixed-speed SCIG- and DFIG-based WFs are

presented to overcome the aforementioned challenges. To overcome the protection problem associated with the operation of distance relays at the terminal of fixed-speed SCIG- or DFIG-based WFs in case of a balanced fault in the backup zone, a new relaying algorithm requiring only local measurements called modified distance element type I is presented. To detect a fault, the modified distance element type I uses the impedance measured at the relay location together with the fault current waveform injected by the SCIG or DFIG. The reliable performance of the modified distance element type I under different types of faults is verified on a 4-bus test system. The obtained results demonstrate the robustness of the modified distance element type I against fault impedances and system disturbances such as power swing and overload conditions.

To overcome the protection challenges associated with the operation of distance relays at the terminal of DFIG-based WFs during large slip operation of DFIGs, a new pilot protection scheme with minimum bandwidth requirements called modified distance element type II is also presented. The developed algorithm relies on the frequency tracking of the fault current injected by the DFIG-based WF. By implementing the modified distance element type II in a 4-bus test system, it is verified that the new relaying algorithm provides reliable protection over the entire length of the transmission line connected to the DFIG-based WF. Moreover, the modified distance element type II accompanied by the modified distance element type I provides proper backup protection for the adjacent lines.

Acknowledgements

First and foremost, I would like to express my sincere gratitude to my supervisor, Professor Sahar Pirooz Azad for her guidance, patience and support throughout my Master studies. Under her supervision, I have learn beyond the boundaries of power and energy systems. It has been my honor to have completed my studies under her supervision and she continues to be my role model in professionalism and class throughout my life.

I would also like to acknowledge the readers of my thesis, Professor Mehrdad Kazerani and Professor Kankar Bhattacharya for their valuable comments to enhance the quality of my work.

Finally, I would like to thank my family for their support and kindness since I was a child until now.

Dedication

This is dedicated to my sweet and loving parents, two strong and gentle souls who taught me to trust in love, believe in hard work and that so much could be done with little.

Table of Contents

List of Tables

List of Figures

Abbreviations

ABG phase-A-to-phase-B-to-ground xii, xiv, 39, 40, 56, 57

AG phase-A-to-ground 33

CISG converter-interfaced synchronous generator 62

DFIG doubly fed induction generator xi, xiii, 2–7, 9–16, 31–35, 37, 38, 41, 43, 45, 46, 48, 49, 51–54, 57–61

FACTS flexible alternating current transmission system 12, 19

FD fault detector 22, 25

FFT fast fourier transform 34

FRT fault ride-through 9

GSC grid-side converter xi, 3–5, 7, 8

IG induction generator 12, 13, 31, 59

IGBT insulated-gate bipolar transistor 6

MPPT maximum power point tracking 4, 7

RSC rotor-side converter xi, 3, 4, 6–8

SCIG squirrel cage induction generator 6, 11–22, 30, 32, 33, 45, 52, 59–61

SFRF stator flux-oriented reference frame 3

SVC static volt-amper reactive compensator 12

UPFC unified power flow controller 12

WF wind farm xiii, 8–22, 30–33, 37, 38, 41, 43, 45, 46, 51–54, 57–61

WT wind turbine xi, 2, 3, 6, 7, 9

List of Symbols

I_{ij}^{ϕ} phase current following from bus i to bus j 20

I_0 zero-sequence current 33

I_A phase-A current phasor magnitude 33

I_{dg} d-axis grid current 5

I_{dr} d-axis rotor current 4

I_{qg} q-axis grid current 5

I_{qr} q-axis rotor current 4

K threshold value 25

K_0 zero-sequence compensation factor 33

P_s^* stator reference active power 4, 7

Q_s^* stator reference reactive power 4

Q_s stator reactive power 4

R_{cb} crowbar resistance 32

R_f fault resistance 20

T' short circuit transient time constant 20

ω_s synchronous angular frequency 20

$\psi_{r,pre}$ pre-fault rotor flux 38

$\psi_{rf,1}$ magnitude of the positive-sequence forced component of the post-fault rotor flux 38

θ fault inception angle 20

θ_i phase-A current phasor angle 33

θ_v phase-A voltage phasor angle 33

f fault current frequency 44

f_{lb} lower bound of the frequency 44

f_{ub} upper bound of the frequency 44

s slip 20

s_{th} slip threshold 44

Chapter 1

Introduction

1.1 Introduction

In the past few decades, many problems associated with the energy crisis, adverse environmental impact of fossil fuels, significant growth of electric demands, limited reserve, and financial restrictions of wholesale markets have arisen worldwide. Under these circumstances, renewable energy sources have been attracting great attention as a technological alternative with the ability to give an effective solution to such problems [1]-[3]. Technological advancements, cost reduction, and governmental incentives have made some renewable energy sources more competitive in the market. Among them, wind energy is one of the fastest-growing renewable energy sources worldwide [1].

The use of wind energy for generating electricity can be traced back to the nineteenth century, when wind energy generators with the size of a few kilowatts were used in the electricity systems [1], [4]. Over time, the size of a wind turbine has significantly increased from a few kilowatts to several megawatts [1], [4]. Moreover, wind turbines can be installed at onshore and offshore locations, where more wind energy can be absorbed by the blades, resulting in higher efficiency [1], [4].

Wind turbines (WTs) are widely installed in today's power systems. Different designs and combinations of generator and power converter lead to a variety of WT configura-

tions and can be divided into three main categories [1]: 1) fixed-speed systems without power converter interface, exclusively using squirrel cage induction generators (SCIGs), 2) variable-speed systems with reduced-capacity converters, using doubly-fed induction generators (DFIGs) and wound rotor induction generators (WRIGs), and 3) variable-speed systems with full-capacity converters, using SCIGs, wound rotor synchronous generators (WRSGs), and permanent magnet synchronous generators (PMSGs). The majority of wind farms (WFs) utilize induction generator (IG)-based WTs among which DFIG-based WTs comprise a considerable share of the installed capacity of wind energy sources worldwide due to their many advantages such as variable speed operation, generator-side active power control ability, and grid-side reactive power control ability [1].

To facilitate a higher penetration of wind power in the power system, various challenges associated with protection, operation, scheduling, and control of WFs should be addressed. One of the critical challenges associated with the high integration of WFs is the impact of WFs on the operation of protection relays in the power system, which may lead to the protection system failure [5]. As some grid codes require WFs to remain connected to the power grid during fault conditions for a specific period [2], WFs contribute to the fault current and change the system fault current characteristics. Such changes in the fault current characteristics considerably affect the operation of the protection system. This dissertation will mostly focus on DFIG-based WFs and will study their negative impacts on the operation of protection relays.

1.2 DFIG-Based WTs

Figure 1.1 depicts the schematic diagram of a DFIG-based WT. The DFIG-based WT is mechanically coupled to the blades through a gearbox and electrically connected to the ac grid via the stator windings. The rotor of the DFIG-based WT is also connected to the ac grid through a back-to-back converter with bidirectional power transfer capability. Depending on the available wind speed, the DFIG-based WT can operate either in sub-synchronous or super-synchronous mode. The slip range of the DFIG-based WT is around $\pm 30\%$ of the synchronous speed [6].

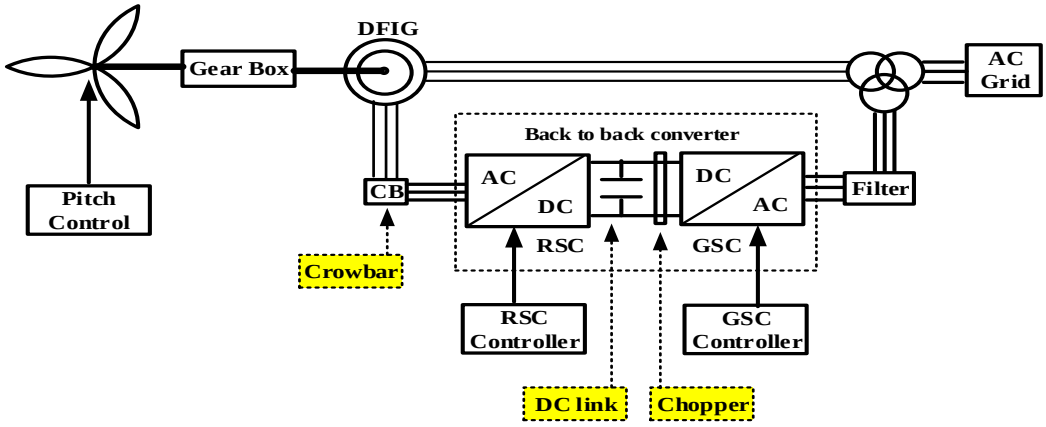

Figure 1.1: Schematic diagram of a DFIG-based WT.

The back-to-back converter consists of a rotor-side converter (RSC), a grid-side converter (GSC), and a dc link capacitor located between the two converters. The stator of the DFIG always injects active power to the ac grid, whereas the active power flows into or out of the DFIG rotor depending on the operation mode of the DFIG. During super-synchronous operation mode, the active power is injected into the ac grid through the back-to-back converter, while the active power flows from the ac grid to the rotor during the sub-synchronous operation mode [7].

Different control strategies are used for controlling DFIG-based WTs under normal conditions and grid disturbances [8], [9]. In modern control systems, vector control in the d-q synchronous reference frame is widely used to control a DFIG-based WT [10]. The control strategy used in this work is based on the stator flux-oriented reference frame (SFRF). In this control strategy, the RSC and GSC controllers are designed in the SFRF, which rotates at the synchronous speed (ω_s).

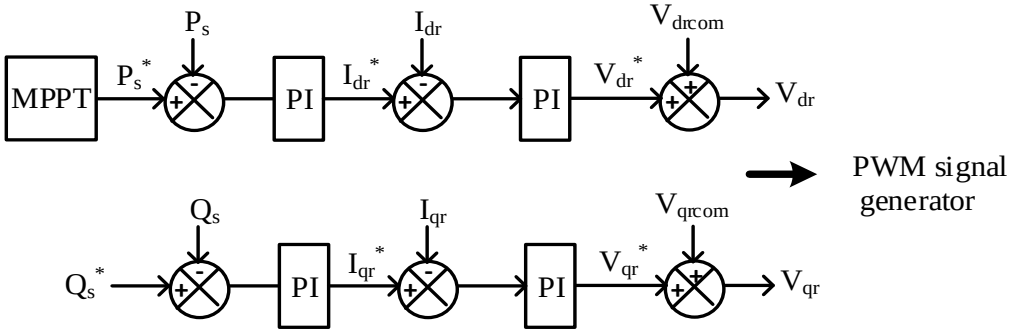

Figure 1.2: Block diagram of the RSC controller.

• **RSC**

In a DFIG, the RSC controller controls the active and reactive powers of the stator through the d-axis and q-axis components of rotor current, respectively. Figure 1.2 illustrates the block diagram of the RSC controller, where I_{dr}, I_{qr}, V_{dr}, and V_{qr} are the dq-axis current and voltage components. In this diagram, the " $*$ " is used to denote reference values. The reference for the active power is obtained based on the maximum power point tracking (MPPT) method. One of the MPPT methods is based on the power versus wind speed curve provided by the wind turbine manufacturer. Such a curve defines the maximum power that the turbine can generate at different wind speeds. In real-time, the wind speed is measured and the active power reference (P_s^*) is generated according to the MPPT profile. The RSC controller controls the reactive power exchange (Q_s) between the stator and the ac grid by selecting the desired reference reactive power (Q_s^*). Further information regarding the mathematical equations, variables, and parameters can be found in [1].

• **GSC**

The main purpose of the GSC controller is to control the voltage of the dc link, V_{dc}, regardless of the direction of the rotor power. For this purpose, the d-axis component of

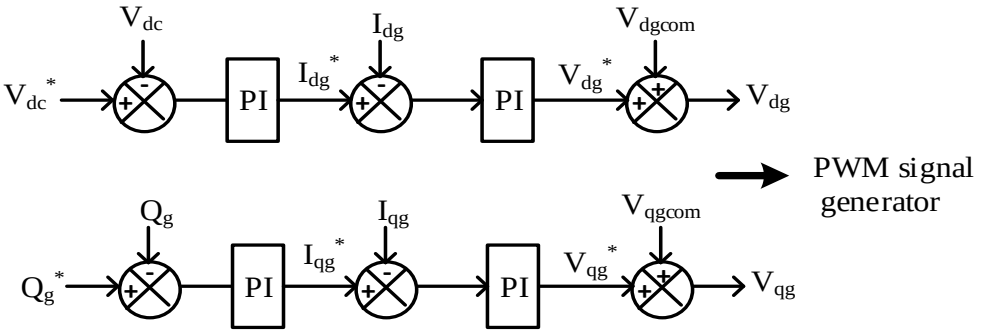

Figure 1.3: Block diagram of the GSC controller.

the grid current is used to control the dc link voltage, whereas the q-axis component of the grid current is used to regulate the reactive power exchange between the GSC and the ac grid. Figure 1.3 illustrates the block diagram of the GSC controller, where I_{dg}, I_{qg}, V_{dg}, and V_{qg} are the dq-axis current and voltage components on the ac side of the GSC. V_{dc} and V_{gcom} are dc link and cross-coupling voltages. During the normal operation of the DFIG, it operates at unity power factor; therefore, the reference reactive power Q_s^* is set to zero [1]. The equations and more details of the variables can be found in [1].

- **Crowbar circuit**

The crowbar circuit is activated when an overcurrent condition occurs on the rotor circuit or an overvoltage condition occurs on the dc link. During the super-synchronous operation of the DFIG, the rotor provides power to the ac grid. If a short-circuit fault occurs on the ac grid close to the generator, the voltage at the generator's terminal collapses and consequently, power cannot be transferred to the ac grid. Therefore, the power is transferred to the dc link, resulting in an overvoltage condition on the dc link.

During the sub-synchronous operation of the generator, power is provided to the rotor circuit from the ac grid. This power is later provided from the rotor to the stator circuit. If a short-circuit fault occurs on the ac grid close to the generator's terminal, the voltage

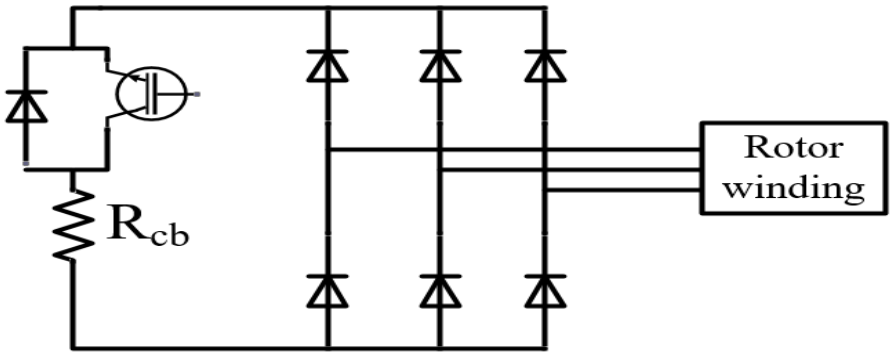

Figure 1.4: Crowbar circuit.

of the stator collapses and the power cannot be delivered to the stator circuit. This will result in stator and rotor currents increasing to large magnitudes. These currents will be only limited by leakage inductances of stator and rotor circuits.

By energizing the crowbar circuit, the RSC is disconnected from the rotor and the crowbar resistor is added in series with the rotor winding. The series-connected resistor will provide a path for the large current to flow and for the rotor power to dissipate. When the crowbar circuit is activated, the DFIG behaves as a squirrel cage induction generator (SCIG). The crowbar circuit implemented in the DFIG-based WT of this thesis is shown in Figure 1.4. The block diagram of the crowbar circuit control is provided in [11].

The value of the crowbar resistance is typically between 1 to 10 times the rotor resistance [12]. When the value of the crowbar resistor is high, the rotor transient current will be dampened immediately. On the other hand, a high crowbar resistor value may lead to overvoltages on the converter. Therefore, a trade-off between these two factors should be considered to select a proper crowbar resistor [12].

- **DC link chopper**

The dc link chopper consists of an insulated-gate bipolar transistor (IGBT)-controlled resistor that is implemented to avoid an overvoltage condition on the dc link capacitor. The schematic of the dc link chopper is illustrated in Figure 1.5. The block diagram of the

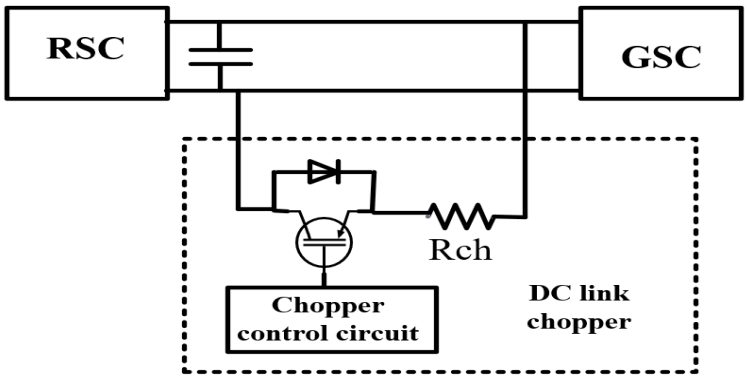

Figure 1.5: dc link chopper.

chopper control is provided in [11].

• **Low pass filter**

In general, power converters generate switching harmonics. To solve this problem, four types of harmonic filters are usually used in the converters, i.e., L, LC, RCL, and LCL [1]. The L and LC filters are normally used for the RSC to reduce the harmonic distortion of the rotor current and voltage, resulting in reducing the harmonic losses in the magnetic core and winding of the rotor. The RCL and LCL filters are usually implemented for the GSC to minimize the impact of the harmonics generated by the back-to-back converter on the ac grid [1]. An RCL filter is implemented for the DFIG-based WT of this thesis and its structure is represented in Figure 1.6. The calculation details of the parameters of a filter are provided in [11].

1.2.1 DFIG-Based WT Model

Figure 1.7 illustrates the control system of the DFIG-based WT that is used in this dissertation. The RSC controller controls the active power of the stator (P_s) through the d-axis component of the rotor current (I_{dr}). The MPPT block is used to generate the reference for the stator active power (P_s^*) based on the wind speed. The MPPT profile is provided by

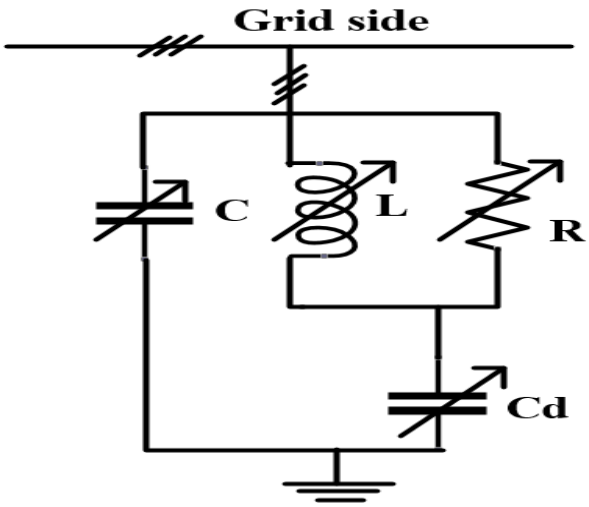

Figure 1.6: RLC filter.

the manufacturer [1]. The RSC controller also controls the reactive power (Q_s) exchange between the ac grid and the stator through q-axis component of the rotor current (I_{qr}) [1]. The abc/dq and dq/abc transformation blocks are implemented to transform the variables in the abc stationary reference frame to the dq synchronous reference frame, and vice versa.

The GSC controller controls the voltage of the dc link (V_{dc}) regardless of the direction of the rotor power. The d-axis component of the current is used to control the voltage of the dc link, and the q-axis component of the current is used to control the reactive power exchange between the ac grid and the GSC [1]. Further information about the controllers along with their variables are provided in [1] and [11].

1.3 Description of the Problems

High penetration of wind power in existing systems requires that a WF remains connected to the power system in case of system disturbances such as short-circuit faults to increase the system reliability and stability [13]. Various grid codes have been developed for the operation of power systems with high penetration of WFs. These grid codes, in particular

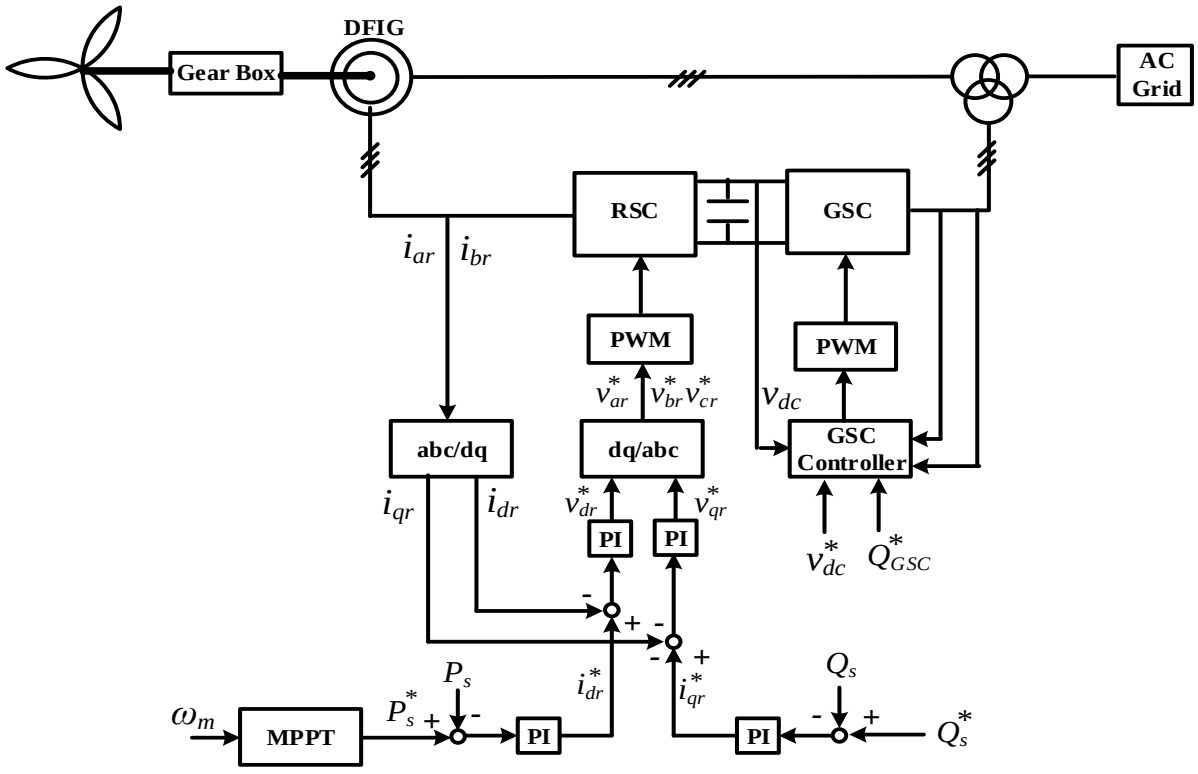

Figure 1.7: DFIG-based WT and its control system [1].

in high voltage systems, require WFs to remain connected to the grid during severe voltage dips for a specified duration. Figure 1.8 illustrates a typical fault ride-through (FRT) curve implemented in the North American grid code. Each point on the curve represents a voltage level and an associated time duration which connected wind power generators must ride through.

High penetration of WFs complying with the FRT requirements can highly affect the operation of protection relays in power systems. In a power system without renewable energy resources, protection systems are designed considering the fact that the systems are supported by synchronous generators. In protection studies of conventional power systems,

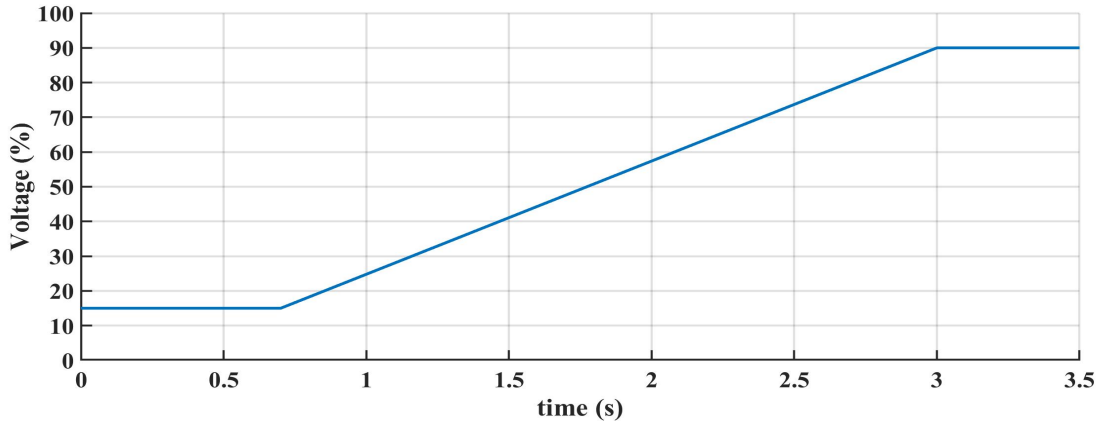

Figure 1.8: Typical FRT curve implemented in the North American grid code [2].

a synchronous generator is modeled as a voltage source in series with an impedance. Such models cannot be used for the fault study of power systems integrated with WFs as they operate as current sources rather than voltage sources [14].

The impact of WFs on the operation of protection relays has been evaluated by many researchers [14]-[24]. [16] provides a comprehensive literature review of the effect of the fault current contribution of distributed generations (DGs), especially WFs, on the protection system performance. [14] and [17] discuss the impact of wind power characteristics on the performance of distance relays in distribution and sub-transmission systems. The authors evaluate the response of conventional protection systems to the operation of different types of WFs during short-circuit faults. In summary, the main protection challenges associated with the protection relays close to a WF can be classified into the following categories: *i*) the fault characteristics of WFs are different from conventional generators [14], [17], *ii*) the limited fault current contribution of WFs is not always sufficient for the proper operation of protection relays [18], [19], *iii*) wind speed variation and the WF source impedance affect the operation of protection relays [20], [21], and *iv*) the fault current frequency of a DFIG-based WF deviates from the nominal frequency during a fault, which affects the operation of protection relays with distance or frequency elements [18]. This dissertation mostly focuses on the DFIG-based WFs and their negative impacts on the

performance of protection systems. Considering different negative impacts of DFIG-based WFs on protection systems due to their large slip range, the short-circuit behaviour of a DFIG is evaluated in two different aspects: 1) close-to-zero slip operation and 2) large slip operation. During close-to-zero slip operation of the DFIG, the short-circuit behaviour of the DFIG is similar to that of a fixed-speed SCIG; therefore, fixed-speed SCIG-based WFs are also evaluated in this dissertation.

One of the main problems is associated with the protection of transmission lines connected to fixed-speed SCIG- or DFIG-based WFs for a balanced fault in the backup zone of the distance relay located at the WF's terminal. When a balanced fault occurs on the adjacent lines to fixed-speed SCIG-based WF, the fault current injected by the fixed-speed SCIG-based WF increases significantly for a short period of time and the impedance calculated at the relay location falls within the protection zone of the distance relay. Then, the current decreases due to a reduction in the machine's air-gap flux [18], which is caused by the significant voltage drop at the SCIG terminal [18]. A few hundred milliseconds after the occurrence of the balanced fault, the fault current reaches zero due to the complete demagnetization of the core of the induction generator and the impedance trajectory finally leaves the protection zone of the distance relay [18]. As a result, the distance relay does not operate correctly for a balanced fault in its backup zone (zone 2) as it should operate after a set time delay [22]. The protection system may face the same problem as that of DFIG-based WFs during close-to-zero slip operation of the DFIG.

Another main problem associated with the protection of a DFIG-based WF arises when the transmission line connected to the DFIG-based WF is protected by distance relays. The performance of a distance relay located at the terminal of DFIG-based WFs will be unreliable and insecure during balanced faults and severe unbalanced faults close to DFIG-based WFs when the DFIGs are operating at a large slip value. When a balanced fault occurs on a transmission line connected to the DFIG-based WF, the crowbar circuit is mostly activated as this is one of the most severe faults in the system. Upon activation of the crowbar circuit located at the rotor side of the back-to-back converter, the fault current passing through the back-to-back converter becomes limited. In this situation, the frequency of the fault current injected by the DFIG-based WF deviates from the synchronous frequency due to slip changes of the DFIG-based WFs in the range of $\pm 30\%$. On

the other hand, the frequency of the voltage at the relay location follows the grid nominal frequency. As a distance relay operates based on the ratio of fundamental frequency voltage and current phasors, the difference in the frequency of the voltage and current measurements provided to the relay during a fault leads to malfunctioning of the distance relay. The protection system may face the same problem as that of a balanced fault in case of a severe unbalanced fault close to a DFIG-based WF [18], [23].

While the negative impacts of induction generator (IG)-based WFs on the protection relays of power systems have been illustrated in the literature, the proposed schemes are not yet very comprehensive. One of the main studies among several current publications on this topic is [18], which proposes a new algorithm for proper operation of a distance relay at the terminal of fixed-speed SCIG- and DFIG-based WFs during a balanced fault. [18] uses the decay in the peak-to-peak amplitude of the fault current to distinguish between fault current fed from a fixed-speed SCIG- or DFIG-based WF and a conventional generator. In the proposed method, fault current direction at the WF substation is detected using the shape of the fault current, while a conventional distance relay at the remote end of the line detects the fault direction by the impedance measurement. This method does not study the performance of distance relays at the terminal of DFIG-based WFs in case of severe unbalanced faults, which leads to frequency deviation of the fault current from the nominal frequency.

[20] proposes a new adaptive setting scheme for a distance relay at the terminal of the WF to protect the transmission line connected to the WF, regardless of the type of the WF. The adaptive setting scheme uses the ratio of local voltage and current at the distance relay location. Using only the local information is the main advantage of the proposed scheme. However, this scheme does not consider the fault response of different types of WFs while designing the relay settings. Furthermore, the adaptive setting scheme fails to protect transmission lines connected to fixed-speed SCIG- and DFIG-based WFs in case of a balanced fault in zone 2 of the distance relay. [21] and [24] present the same adaptive setting scheme for protecting the lines connected to the WFs, with the only difference that they also consider the impact of flexible alternating current transmission system (FACTS) devices such as unified power flow controller (UPFC), [24], and static volt-amper reactive compensator (SVC), [21], on the distance relay characteristics. However,

the aforementioned problems associated with [20] still exist in these protection schemes.

In [15], a distance differential method is proposed for the protection of lines connected to WFs. This method assumes that current and voltage measurements from the remote end of the transmission line are available at the relay location. Then, by calculating the active power at both ends of the line, the fault resistance and consequently the fault location is estimated. The main drawback of implementing this scheme is that it requires high bandwidth communication infrastructure to protect the line connected to the WF.

1.4 Motivation

WFs' contribution to the fault current can negatively affect the protection of power systems. Among different types of WFs, fixed-speed SCIG- and DFIG-based WFs encompass a high percentage of the installed capacity of wind power plants in power systems. The DFIG typically operates about 30% below or above synchronous speed, which is sufficient for most wind speed conditions. It also enables to control the generator-side active power and the grid-side reactive power [1]. The fixed-speed SCIG, on the other hand, is simple and rugged in construction, relatively inexpensive and requires minimum maintenance [1]. The main focus of this dissertation is on the response of DFIG-based WFs to different types of faults. However, the impact of fixed-speed SCIG-based WFs on the protection system is also evaluated due to the same short-circuit behaviour of DFIG and fixed-speed SCIG during the close-to-zero slip operation of the DFIG.

Since the response of IG-based WFs to short-circuit faults are not similar to that of conventional generators, the conventional protection relays close to WFs may fail to operate properly or even lose their coordination with downstream relays in case of a fault. The focus of this thesis is on the performance of distance relays that are located at the terminal of WFs.

As mentioned in Section 1.3, a few papers have evaluated the negative effects of IG-based WFs on the operation of conventional protection relays and have proposed new schemes to tackle the protection challenges [14]-[24]. The main drawbacks of the existing schemes for the protection of lines connected to the fixed-speed SCIG- and DFIG-based

WFs include *i*) high bandwidth communication requirement for exchanging information between the relays at two ends of the line connected to the WF [15], *ii*) inability to operate reliably in case of severe unbalanced faults close to the DFIG-based WF [18], *iii*) continuous information requirement of the fixed-speed SCIG- and DFIG-based WFs, i.e. wind speed, to provide an adaptive relaying setting for the WF-side relay [20]-[21], [24], and *iv*) failure to provide proper backup protection for the downstream relays in case of a balanced fault in zone 2 of the DFIG- or SCIG-side relay [20]-[21], [24]. Hence, further research should be conducted to overcome the aforementioned challenges.

1.5 Contributions

The contributions of this dissertation fall into two main categories: *i*) the comprehensive explanation of the failure of relays located at the terminal of fixed-speed SCIG- and DFIG-based WFs using the mathematical equations and the simulation results, and *ii*) the development of relaying algorithms to address these protection challenges.

1.5.1 Relay Failures

The followings are the main relay failures that this dissertation discusses:

1. A conventional distance relay located at a fixed-speed SCIG or DFIG terminal fails to operate correctly for a balanced fault in its backup zone (zone 2). Depending on the impedance trajectory measured by the SCIG- or DFIG-side relay for a balanced fault in zone 2, it will lose its coordination with the downstream relays if the impedance trajectory enters zone 1, or it cannot provide proper backup protection for the adjacent line if the impedance trajectory leaves the relay's zones. This problem happens for the distance relay located at the terminal of a DFIG during close-to-zero slip operation of the DFIG.

2. The performance of a distance relay located at the terminal of a DFIG-based WF will be unreliable and insecure during balanced faults due to the frequency deviation

of the fault current from the nominal frequency. This condition will be problematic in case of a balanced fault on the adjacent line, where it is protected by zone 2 of the distance relay. In this situation, the impedance trajectory may enter zone 1, which results in loss of coordination between the distance relay at the DFIG terminal and the downstream relays.

1.5.2 Modified Distance Elements

This dissertation presents the following solutions for the aforementioned relay failures:

1. To overcome the problem associated with the unreliable operation of a distance relay at the terminal of a fixed-speed SCIG or DFIG-based WF for a balanced fault in zone 2, a new relaying algorithm called modified distance element type I based on only local measurements at the relay location is presented to properly detect and identify balanced and unbalanced faults in the relay protection zones. By employing the modified distance element type I in the SCIG or DFIG-side relay, the relay can provide instantaneous protection for faults in zone 1 as well as reliable backup protection for any faults in zone 2 of the relay. The main advantages of the modified distance element type I include, *i*) the ability to distinguish faults from system disturbances, *ii*) requiring only local measurements at the relay location, and *iii*) robustness against different system disturbances such as power swings and load encroachments.

2. To overcome the problem associated with the unreliable operation of a distance relay at the terminal of a DFIG-based WF during faults, a new pilot protection scheme called modified distance element type II is presented. The modified distance element type II *i*) distinguishes faults from other system disturbances, *ii*) provides reliable protection over the entire length of transmission line connected to the DFIG-based WF, *iii*) requires minimum communication bandwidth, and *iv*) is robust against different systems disturbances such as power swings and load encroachments.

1.6 Outline

The rest of this dissertation is organized as follows. In Chapter 2, the performance of a distance relay at the terminal of SCIG-based WFs for different types of faults is evaluated. After demonstrating the negative impact of the fixed-speed SCIG-based WFs on the operation of conventional distance relays, a new relaying algorithm is presented to reliably protect the transmission line connected to a fixed-speed SCIG-based WF. Moreover, the reliable performance of the new relaying algorithm is demonstrated by implementing it in a 4-bus test system. The response of DFIG-based WFs to short-circuit faults is discussed in Chapter 3. In Chapter 3, a new relaying algorithm is presented to reliably protect the transmission line connected to a DFIG-based WF. The reliable performance of the developed relaying algorithm is demonstrated by employing the algorithm in a 4-bus test system. Chapter 4 provides the conclusions and directions for future work.

Chapter 2

Fixed-Speed SCIG-Based Wind Farms

2.1 Introduction

The main problem associated with the protection of fixed-speed SCIG-based WF arises when the transmission line connected to the SCIG is protected by a distance relay. When a balanced fault occurs on the adjacent lines to SCIG, the fault current injected by the SCIG increases significantly for a short period of time and the impedance calculated at the relay location falls within the protection zone of the distance relay. Then, the current decreases due to a reduction in the machine's air-gap flux [18], which is caused by the significant voltage drop at the SCIG terminal [18]. A few hundred milliseconds after the occurrence of the balanced fault, the fault current reaches zero due to the complete demagnetization of the core of the induction generator and the impedance trajectory finally leaves the protection zone of the distance relay [18]. As a result, the distance relay does not operate correctly for a balanced fault in its backup zone (zone 2) as it should operate after a set time delay [22]. This problem also happens for the distance relay located at the terminal of a DFIG during close-to-zero slip operation of the DFIG. This will be addressed in Chapter 3.

This Chapter proposes a new relaying algorithm called modified distance element type I based on the local measurements at the relay location to overcome the problems regarding the protection of transmission lines connected to fixed-speed SCIG-based WFs in the presence of balanced and unbalanced faults. The relay under investigation is located at the terminal of the fixed-speed SCIG-based WF. The modified distance element type I uses the impedance measured at the relay location together with phase fault current waveforms injected by the SCIG to detect the faults. After the occurrence of a fault, the modified distance element type I first distinguishes balanced faults from unbalanced faults and then it will use the apparent impedance to differentiate between balanced faults in zone 1 and zone 2 of the relay. Then, the damping characteristics of the fault current injected by the SCIG will be used to provide proper coordination with the downstream relays. The performance of the modified distance element type I is verified on a 4-bus test system. The obtained results demonstrate the robustness of the modified distance element type I against fault impedances and system disturbances such as power swings and overload conditions.

2.2 Test System

Figure 2.1 shows the single-line diagram of the 4-bus test system used in the studies of this dissertation. In this system, the fixed-speed SCIG-based WF is connected to bus i, and two identical sources with the same characteristics are connected to bus k and l. The fixed-speed SCIG-based WF is represented with an equivalent SCIG WT and the equivalent impedance of all interconnecting cables [18], [25]. Transformers installed at the SCIG terminal and the sources have the same parameters. The parameters of the system are provided in Table 2.1.

2.3 Problem Statement

Distance relays are the most commonly used types of protection relays in transmission systems. A distance relay operates based on the measured impedance between the relay

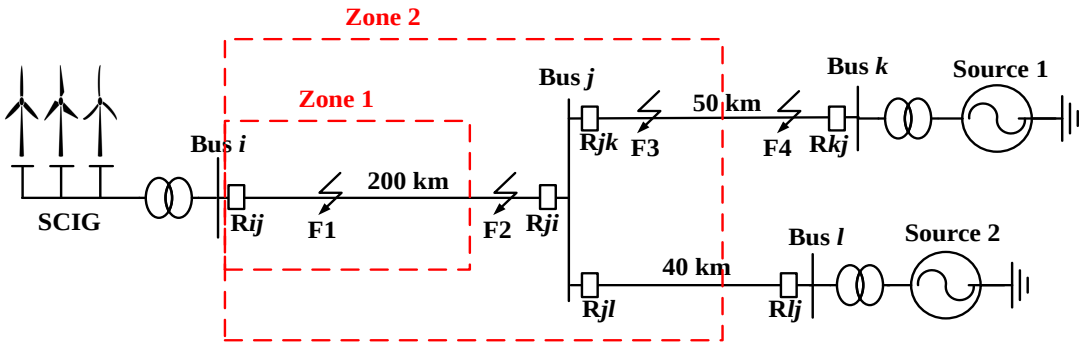

Figure 2.1: Single-line diagram of the test system.

and the fault location and operates if the fault occurs within its protection zones. The apparent impedance calculated by the distance relay can be calculated as [20]

$$Z = Z_{line} + Z_{error} \ , \tag{2.1}$$

where Z_{line} is the line positive-sequence impedance between the relay and the fault location. Z_{error} is the error term, which depends on several main factors such as the fault resistance [26], the currents fed from the adjacent lines [26], and the shunt current and series voltage injection by FACTS devices [27]. In conventional power systems, Z_{error} is mostly insignificant. However, this error can be problematic for the operation of a distance relay located at the terminal of the fixed-speed SCIG-based WF when a balanced fault occurs on the adjacent lines [18]. The rest of this section will focus on the impact of the location of the fault, i.e., internal balanced faults and external balanced faults, on Z_{error}.

2.3.1 Internal Balanced Faults (F1 and F2)

The apparent impedance calculated by the relay located at the SCIG terminal (Rij) in the phasor domain for an internal balanced fault is given by

$$Z = Z_{if} + R_f \frac{I_{ij}^{\phi} + I_{kj}^{\phi} + I_{lj}^{\phi}}{I_{ij}^{\phi}} = Z_{if} + Z_{error}^{int} \ , \tag{2.2}$$

Table 2.1: Parameters of the test system.

Component	Parameter	Value
Fixed-Speed SCIG	Apparent power	25 MVA
	Nominal voltage	480 V
	Stator resistance	0.09 p.u.
	Rotor resistance	0.004 p.u.
	Magnetizing inductance	6.5 p.u.
	Stator and rotor inductance	0.04 p.u.
Source	Nominal voltage	480 V
	Positive- and negative-sequence impedances	$1\angle 85°$ p.u.
	Zero-sequence impedance	$1.5\angle 85°$ p.u.
Transformer	Apparent power	30 MVA
	Nominal voltages	480/69000 ΔYg
	Leakage inductance	0.1 p.u.
Transmission line	Positive- and negative-sequence impedances	$0.144\angle 86°$ Ω/km
	Zero-sequence impedance	$0.437\angle 86°$ Ω/km

where Z_{if} is the positive-sequence impedance of the line between Rij and the fault location, Z_{error}^{int} is the impedance error, I_{ij}^{ϕ} is the phase current flowing from bus i to bus j, and R_f is the fault resistance. According to (2.2), the error term depends on the fault resistance, the fault current fed from the SCIG (I_{ij}^{ϕ}), and the currents injected by sources 1 and 2 (I_{kj}^{ϕ} and I_{lj}^{ϕ}). Regardless of the fault location (internal or external), the current injected by the fixed-speed SCIG-based WF during a balanced fault consists of a decaying ac and a decaying dc component [18], [28]:

$$i_s(t) = \frac{V_{max}}{1-s}\left(\frac{1}{X'} - \frac{1}{X_{\sigma s} + 1.5X_{ms}}\right)e^{-\frac{t}{T'}} \times \cos((1-s)\omega_s t + \theta) + \frac{V_{max}}{1-s}\left[\frac{1}{X'}e^{-\frac{t}{T_s}} \times \cos(\theta)\right], \quad (2.3)$$

where T' and T_s are the short-circuit transient and the stator time constants, respectively. V_{max}, X', X_{ms}, $X_{\sigma s}$, ω_s, s, and θ are the voltage amplitude, transient reactance, magnetizing reactance, stator leakage reactance, synchronous speed, machine slip, and fault inception angle, respectively.

For a few cycles after the fault occurrence, the SCIG can be modeled as a voltage source in series with a transient impedance [29], based on the constant flux linkage theorem presented in [30]. There will be a considerable increase in the fault current during this short time period. Then, since the air-gap flux of the fixed-speed SCIG-based WF reduces due to the voltage drop at the machine terminal, both ac and dc components of the fault current start to decrease with a large damping factor [18]. Finally, the fault current reaches zero after several hundred milliseconds according to (2.3). Based on (2.2), the fault current fed by SCIG has a significant impact on the impedance error calculated by Rij. For a balanced fault at F2 with a non-zero fault resistance, after several hundred milliseconds from the fault instant, Z_{error}^{int} measured by Rij will be substantial due to the small value in the denominator of Z_{error}^{int}. Therefore, the impedance trajectory will leave zone 2 of Rij before it operates. As a result, Rij will not be able to protect the remote end of the line ij, which is covered by zone 2 [28], [18].

For a solid balanced fault F2, Z_{error}^{int} is zero. Also, faults in the primary protection zone of the relay such as F1 will be detected correctly, due to the high magnitude of the fault current during the transient period, which results in the impedance entering zone 1 immediately after the onset of the fault. For an unbalanced fault, the impedance trajectory will not leave zone 2 as the current magnitude does not immediately decay to zero. The reason is that the air-gap flux during an unbalanced fault scenario does not decrease as much as a balanced fault scenario due to the higher voltage values in the healthy phases [31].

2.3.2 External Balanced Faults (F3 and F4)

For an external fault, the impedance calculated by Rij is

$$Z = Z_{if} + Z_{jF}(\frac{I_{ij}^{\phi} + I_{lj}^{\phi}}{I_{ij}^{\phi}}) + R_f \frac{I_{ij}^{\phi} + I_{kj}^{\phi} + I_{lj}^{\phi}}{I_{ij}^{\phi}} = Z_{if} + Z_{jF} M_I + Z_{error}^{ext} \ , \qquad (2.4)$$

where Z_{error}^{ext} is the impedance error due to a balanced fault and M_I is the impedance error due to the infeed.

According to (2.4), the impedance error measured by Rij includes two current-dependent terms, $Z_{jF}M_I$ and Z_{error}^{ext}. Due to the $Z_{jF}M_I$ term, the impedance exhibits significant variations for both solid- and non-solid faults after several hundred milliseconds from the fault instant. Due to the substantial error in the measured impedance by Rij during solid- and non-solid faults, Rij may not provide a reliable backup protection for a part of line jk and line jl, which must be protected by the zone 2 element.

2.4 Modified Distance Element Type I

In this section, a new relaying algorithm called modified distance element type I is presented, which provides reliable protection against balanced and unbalanced faults for relays located at the terminal of fixed-speed SCIG-based WFs. The developed relay operates based on the combination of conventional distance element [32], for detecting unbalanced faults, and a newly proposed technique for detecting balanced faults. The modified distance element type I is based on the impedance measured by the distance relay and the phase fault current waveform of the SCIG. The relay located at the remote end of the line is a conventional distance relay, which can reliably operate for all types of faults. The modified distance element type I is shown in Figure 2.2.

2.4.1 Fault Detection

The fault detector (FD) unit distinguishes faults from the other types of disturbances in the system. The implemented FD unit is similar to the one developed in [33], where a one-cycle moving sum of the current samples immediately after the occurrence of the disturbance is calculated. The symmetrical nature of the current waveforms during the normal operation of the power system (even during power swing and overload conditions) results in the moving sum to be around zero, while it deviates from zero during faults.

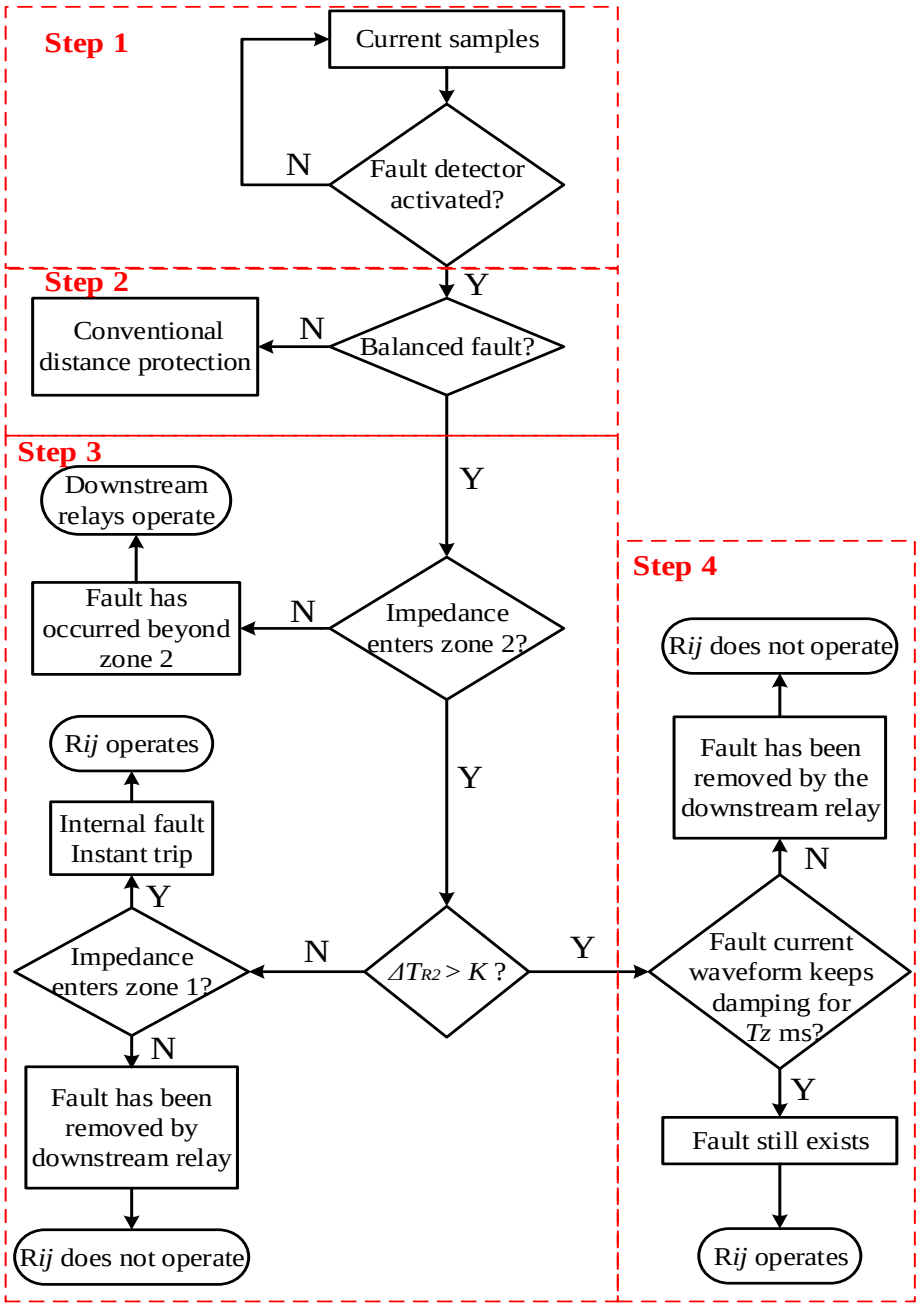

Figure 2.2: Modified distance element type I for Rij operation.

2.4.2 Balanced Fault Detection

In this step, a fault type classifier is applied to determine whether the fault is balanced or unbalanced. To achieve this, the following index is defined

$$FDC = \frac{NS_c}{PS_c}\ , \tag{2.5}$$

where NS_c and PS_c are the negative- and positive-sequence components of the current, respectively.

For balanced faults, FDC value is close to zero, while it deviates from zero during unbalanced faults. Therefore, the balanced faults and unbalanced faults can be distinguished by determining a suitable threshold for FDC. Conventional distance relaying algorithms such as [20] and [32] can be used in Rij to provide reliable protection against unbalanced faults.

2.4.3 Impedance Zone Detection and Relay Coordination

In this step, the impedance measured by the relay is used to determine whether a balanced fault has occurred in zones 1 and 2 of Rij. If the impedance trajectory enters zone 2, even for a short period of time, it will be associated with a balanced fault in zone 1 or zone 2 of the relay.

According to (2.2) and (2.3), since the magnitude of the fault current of the SCIG is substantial for a few cycles after the onset of the fault, the impedance trajectory will remain in zone 2 without entering zone 1 for a time period ΔT_{R2}. Comparison of ΔT_{R2} against a threshold serves as the main criterion to distinguish between balanced faults in zone 1 and zone 2. To achieve this, ΔT_{R2} is compared with a threshold K if i) $\Delta T_{R2} \leq K$ and the impedance trajectory enters zone 1, the fault is detected to be in zone 1, ii) $\Delta T_{R2} \leq K$ and the impedance trajectory leaves zones 1 and 2, the fault is identified and cleared by a downstream relay (e.g. Rjk or Rjl), and iii) $\Delta T_{R2} \geq K$, the fault is detected to be in zone 2.

To ensure this criterion can identify all balanced faults in zone 2, the shortest time period for which the impedance trajectory remains in zone 2 for an uncleared balanced fault is determined. This critical fault scenario is associated with a high impedance balanced fault at the end of zone 2, which is not cleared by the downstream relay (Rjk or Rjl). ΔT_{R2} for the critical fault scenario is used to select the relay threshold K.

2.4.4 Uncleared Zone 2 Fault Detection

If the impedance trajectory remains within zone 2 for more than K ms, it indicates that the location of the fault is in the second zone (e.g., F2 or F3). According to (2.2) and (2.3), although the impedance trajectory will remain within zone 2 for more than K ms, it will leave zone 2 before the time delay settings of this zone ($Tz\ ms$) and therefore, the fault will not be cleared by a conventional distance relay. To solve this problem, the relay will use the fault current damping characteristic. If the current waveform continues to damp out for Tz ms after the onset of the fault, the relay will operate after the set time delay. However, for a fault already removed by the downstream relays, the fault current does not damp out anymore.

2.5 Simulation Results

To evaluate the performance of the modified distance element type I, the system shown in Figure 2.1 is simulated in the PSCAD/EMTDC environment and the waveforms are processed in the MATLAB environment. The transposed transmission lines are simulated using the frequency-dependent line model. The first zone of Rij is set to protect 85% of line ij, and the second zone of Rij will cover line ij and 50% of the longest adjacent line (line jk).

First, the algorithm used in FD unit is evaluated by studying the test system under three scenarios including short-circuit faults (balanced and phase-A-to-ground faults at 95% of line ij at $t = 4\ s$ with $Rf = 1\ \Omega$), power swings, and overloads (adding a new load with the size of 100 MW and 25 MVAR to bus j at $t = 4\ s$). In order to create a power

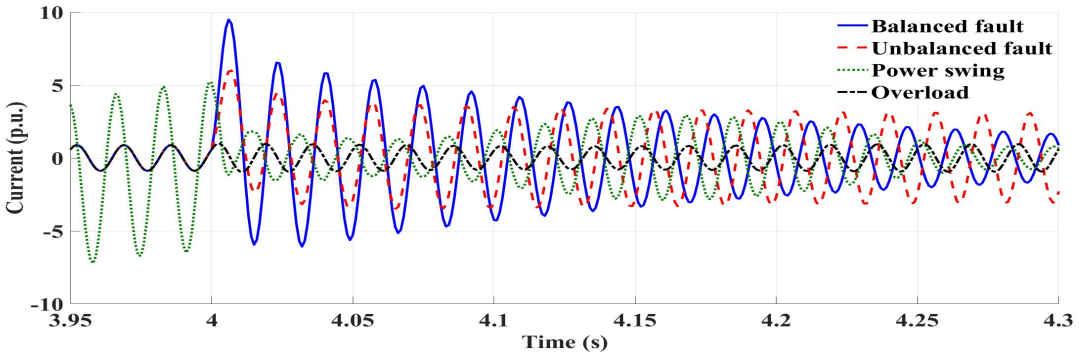

Figure 2.3: Fault current waveforms of phase-A before and after the occurrence of disturbances and faults.

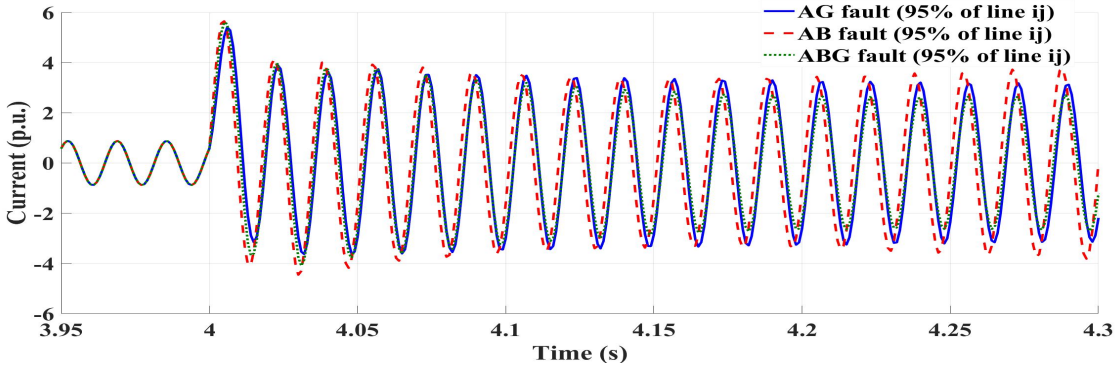

Figure 2.4: Fault current waveforms for unbalanced faults at 95% of line ij with $Rf = 1\ \Omega$.

swing phenomenon in the system, a transmission line parallel with line ij is added to the system. Then, a balanced fault in the middle of the new line is initiated at $t = 3.9\ s$ and is removed at $t = 4\ s$ by opening the circuit breakers located at both ends of the new line. The current waveforms fed by the SCIG for these three scenarios are shown in Figure 2.3. The current waveforms associated with the power swing and overload conditions are almost symmetric; however, the fault current waveform is asymmetric due to the existence of the decaying dc in the waveform. The sum of samples taken over one cycle after the onset of the disturbances is around zero (0.026 $p.u.$ and 0.064 $p.u.$) for power swing and overload scenarios, while it is substantial (5.393 $p.u.$ and 4.154 $p.u.$) for balanced and unbalanced

Table 2.2: ΔT_{R2} for balanced faults at different locations.

Fault resistance (Ω)	Fault location %	ΔT_{R2} (ms)
0.2	90% of line ij	112
	100% of line ij	108
	20% of line jk	82
	30% of line jk	73
	50% of line jk	61
1	90% of line ij	93
	100% of line ij	84
	20% of line jk	73
	30% of line jk	59
	50% of line jk	43

faults.

A threshold value of 0.2, which is larger than maximum value for the balanced faults in the system (0.071), is selected for FDC to distinguish between balanced and unbalanced faults. As shown in Figure 2.4, after around 150 ms from the onset of the fault, the magnitude of the unbalanced current is larger than that of the balanced fault. This will result in the impedance trajectory associated with the unbalanced fault remaining within zone 2 of the distance relay and consequently being detected by a conventional distance element. Figure 2.4 also demonstrates the high magnitude of current for various unbalanced faults.

For the test system of Figure 2.1, the threshold K is determined by applying balanced faults at different locations in zone 2 of Rij to identify the critical fault scenario. ΔT_{R2} for several unbalanced faults is provided in Table 2.2. According to Table 2.2, the critical fault scenario with minimum ΔT_{R2} is associated with the fault at 50% of line jk with $Rf = 1\ \Omega$. During the critical fault scenario, the impedance stays in zone 2 for 43 ms; therefore, $K = 40$ ms is selected.

The impedance trajectories calculated by Rij for the balanced faults F1, F2, F3, and

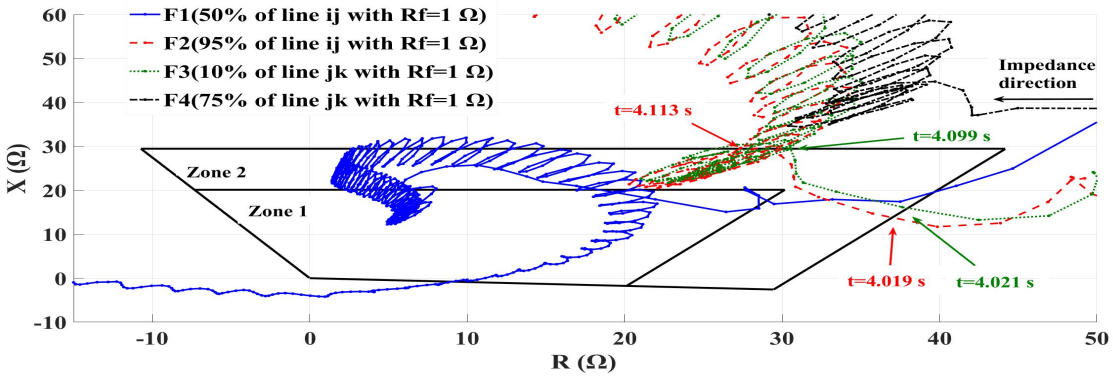

Figure 2.5: Impedance trajectories in the presence of balanced faults at four different locations with $Rf = 1\ \Omega$.

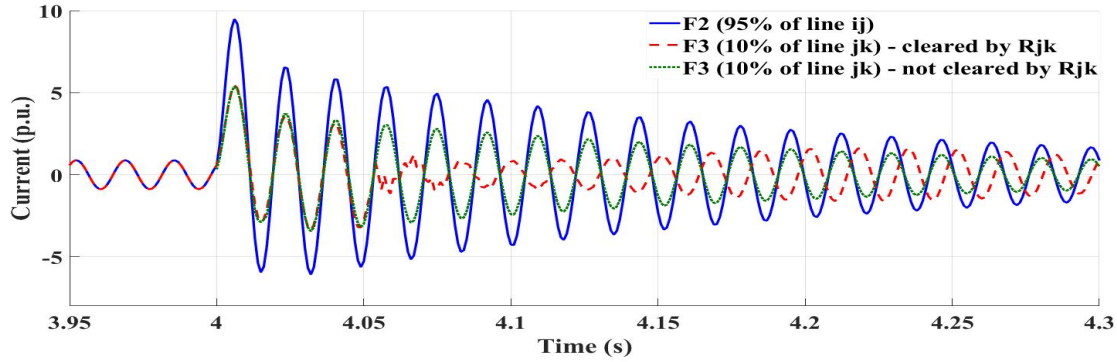

Figure 2.6: Fault currents associated with F2 and F3 (balanced faults).

F4 are depicted in Figure 2.5. The faults occur at $t = 4\ s$ and they are not cleared during the simulation. For F1, the impedance enters zone 1 immediately after the occurrence of the fault, resulting in the proper operation of the relay. For F4, the impedance trajectory does not enter zones 1 and 2 and Rij does not detect the fault. However, for F2 and F3, the impedance trajectories correctly enter zone 2 and remain within zone 2 for 94 ms and 78 ms, respectively, and then leave zone 2 before the time delay setting for the backup zone ($Tz = 300\ ms$). Since the impedance trajectories for F2 and F3 remain in zone 2 for more than 40 ms, the fault current waveform is examined to provide proper coordination between Rij and downstream relays (Rjk and Rjl).

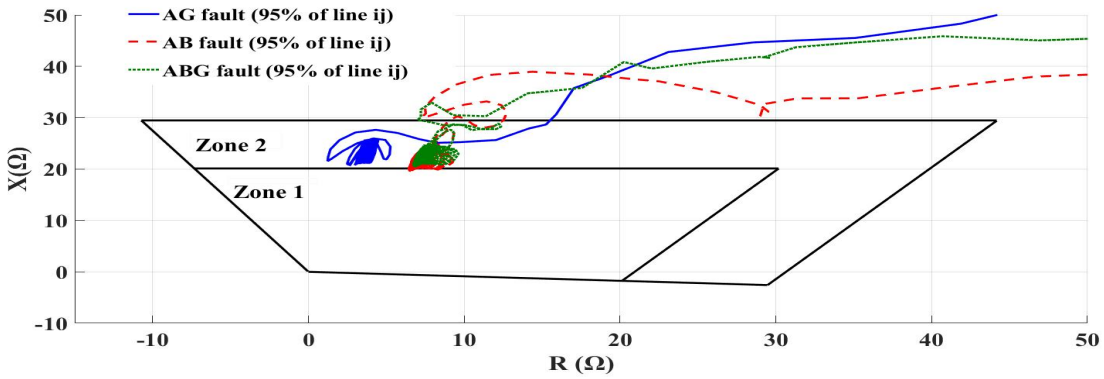

Figure 2.7: Impedance trajectories for unbalanced faults at 95% of line ij with $Rf = 1\ \Omega$.

Figure 2.6 shows the fault current associated with F2 and F3 (balanced faults). The current waveform associated with F2 keeps damping for more than $Tz = 300$ ms, resulting in the proper operation of Rij after this time delay. On the other hand, the current waveform associated with F3 stops damping due to the fault clearance by the downstream relay Rjk and therefore, Rij will not operate. If Rjk fails to detect F3, the current waveform continues damping for more than 300 ms and Rij will operate correctly as the backup for Rjk to clear the fault. Figure 2.7 shows that the impedance trajectories associated with the unbalanced faults remain within zone 2 for more than 300 ms and therefore, the conventional distance elements are able to detect the unbalanced faults and operate correctly.

The impedance in the R-X plane may follow different paths after the occurrence of a balanced fault, which depend on various factors such as the fault impedance. The robustness of the modified distance element type I against the fault impedance is examined in Figure 2.8. Figure 2.8 shows the impedance trajectory measured by Rij for three different balanced faults. For the balanced fault at 95% of line ij with $Rf = 0$, the impedance enters zone 2 and remains within zone 2 until it is cleared. For the balanced fault at 95% of line ij with $Rf = 1\ \Omega$, the impedance trajectory remains within zone 2 for 94 ms and then leaves the protection zones. Also, for the balanced fault at 95% of line ij with $Rf = 0.1\ \Omega$, the impedance trajectory remains within zone 2 for 114 ms and then enters zone 1. The modified distance element type I works well for all these fault scenarios

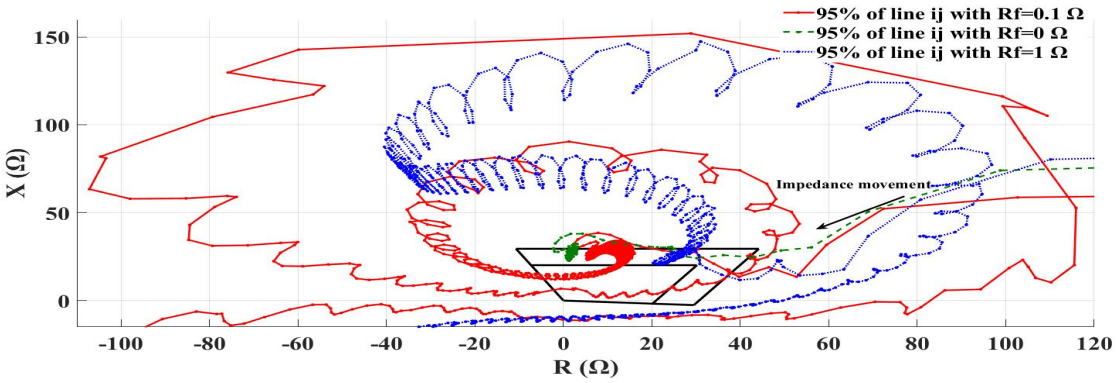

Figure 2.8: Impedance trajectories for three different fault scenarios.

as the impedance trajectory remains for more than $K = 40$ ms within zone 2. After $K = 40$ ms, Rij will operate based on the damping characteristics of the fault current waveform.

2.6 Summary

Since a distance relay located at the terminal of an fixed-speed SCIG-based WF may not operate correctly for a balanced fault within zone 2, a new relaying algorithm is developed based on the impedance measured by the relay and the damping characteristics of the phase fault current injected by the SCIG. The modified distance element type I 1) distinguishes faults from other system disturbances, 2) differentiates between balanced and unbalanced faults, and 3) reliably detects faults in the different zones of the relay. The performance of the modified distance element type I is examined on a 4-bus test system. The simulation results show that the modified distance element type I detects balanced and unbalanced faults in the two protection zones of the relay and generates the correct trip signal. Furthermore, this method does not maloperate during system disturbances such as power swing and overload conditions. Simplicity in the design, local measurement requirement and robustness against fault impedance and fault location are the main advantages of the modified distance element type I.

Chapter 3

DFIG-Based Wind Farms

3.1 Introduction

IG-based WFs are increasingly being integrated into the power systems at different voltage levels, and the protection of the transmission lines with the addition of these WFs is becoming more complicated. This chapter describes one of the challenges associated with the protection of transmission lines connected to the DFIG-based WFs during short-circuit faults. It is shown that the performance of distance relays located at the terminal of DFIG-based WFs will be unreliable and insecure during balanced faults and severe unbalanced faults. The malfunctioning of the relays are due to the differences in the frequency of the voltage and current measurements provided to the relay during a fault, and this arises from the slip changes of the DFIGs in the range of $\pm 30\%$.

In this chapter, a new relaying algorithm called modified distance element type II is presented to address the discussed protection challenge. The modified distance element type II is based on the time-frequency curves extracted from the fault currents measured at the distance relays located at the two ends of a transmission line connected to a DFIG-based WF. The modified distance element type II consists of two components: *i*) fault detection and *ii*) fault type identification. The simulation results of this Chapter verify the merits of the modified distance element type II in successful detection and identification of various fault scenarios.

3.2 Problem Statement

3.2.1 Balanced Faults

When a balanced fault occurs on an adjacent transmission line to the DFIG-based WF, the crowbar circuit is mostly activated as this is one of the most severe faults in the system. Upon activation of the crowbar circuit located at the rotor side of the back-to-back converter, the fault current passing through the back-to-back converter during a balanced fault becomes limited. When the crowbar circuit is activated, the short-circuit behavior of the DFIG-based WF will be similar to that of a fixed-speed SCIG-based WF as discussed in Chapter 2 [34]. However, the main differences between the fault response of the two types of WFs are associated with the effect of the crowbar circuit and the larger slip range of the DFIG. The balanced fault current of a DFIG-based WF is [28]

$$i_s(t) = \frac{V_{max}}{(1-s)\sqrt{X'^2 + R_{cb}^2}}[e^{-\frac{t}{T'_{cb}}} \times \cos((1-s)\omega_s t + \theta - \frac{\pi}{2}) - e^{-\frac{t}{T_s}} \cos(\theta - \frac{\pi}{2})] \ , \quad (3.1)$$

$$T_s = \frac{X'}{\omega_s R_s} \ , \quad (3.2)$$

$$T'_{cb} = \frac{X'}{\omega_s(R_r + R_{cb})} \ , \quad (3.3)$$

where R_{cb} is the crowbar resistance of the DFIG-based WF. The fault current injected into the line from the ac grid is [28]

$$i_g(t) = \frac{V_{max}}{Z}[\sin(\omega_s t - \theta) - \sin(\theta) \times e^{-\frac{t}{T}}] \ , \quad (3.4)$$

As the slip of an fixed-speed SCIG is near zero, the $(1-s)$ term in (2.3) can be neglected, resulting in a fault current with the nominal grid frequency of ω_s. In contrast, as the slip of a DFIG changes in the range of $\pm 30\%$, the $(1-s)$ term will be considerable. As a result, the fault current frequency injected by a DFIG-based WF changes in the range of

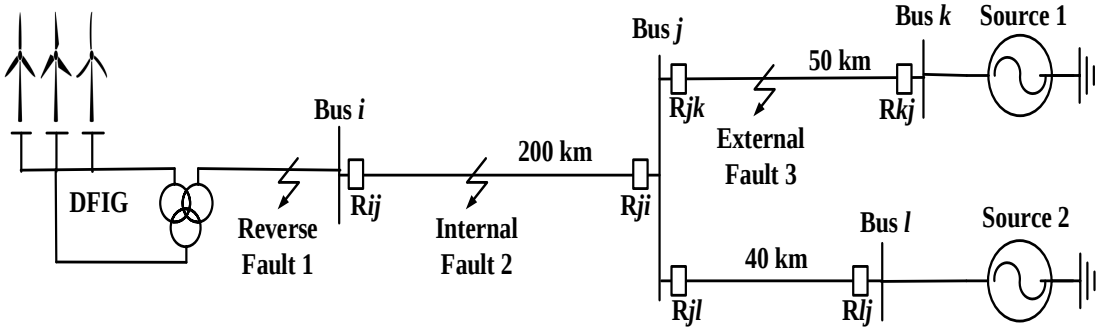

Figure 3.1: Single-line diagram of the test system.

42-78 Hz for a 60 Hz system. On the other hand, during a balanced fault, the voltage frequency captured at the relay location follows the frequency of the ac grid and remains within a narrow margin of the nominal frequency. Therefore, the frequency of voltage and current measured at the relay location will be different during the non-zero slip operation of the DFIG. This difference between the frequency of voltage and current negatively affects the performance of a distance relay. To illustrate more, the impedance measured by the phase-A-to-ground (AG) element of a distance relay is calculated as

$$Z_{AG} = \frac{V_A \angle \theta_v}{I_A \angle \theta_i + K_0 I_0} \,, \tag{3.5}$$

where $V_A\angle\theta_v$ and $I_A\angle\theta_i$ are the fundamental frequency phasors of the phase-A voltage and current, respectively. I_0 is the zero-sequence current, and K_0 is the zero-sequence compensation factor [32]. The distance relay operates based on the ratio of the voltage and current phasors measured at the relay location. However, due to the deviation of the fault current frequency from the nominal frequency, the impedance value calculated by (3.5) will not be an accurate estimation of the impedance between the fault and relay location, which will result in the maloperation of the distance relay.

The test system is shown in Figure 3.1. To form this test system, the fixed-speed SCIG-based WF in the test system of Section 2 is replaced by a DFIG-based WF. The DFIG-based WF is represented with an equivalent DFIG-based WT and the equivalent impedance of all interconnecting cables [18], [25]. The studies are based on time-domain

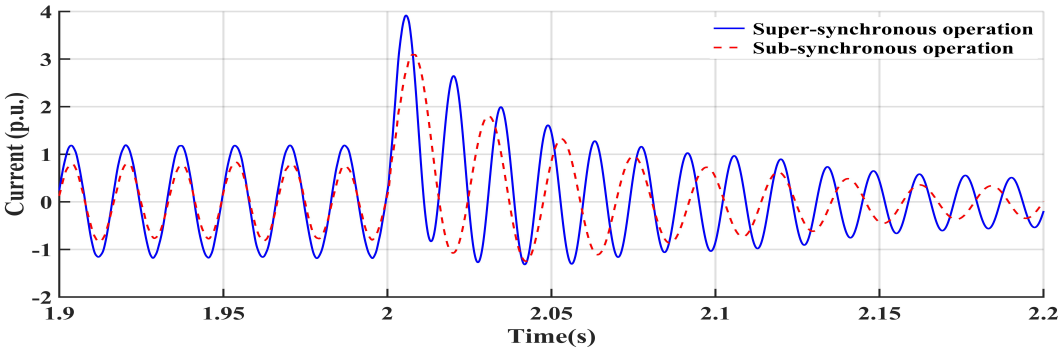

Figure 3.2: Phase-A current at relay Rij after a balanced fault on line jk for super-synchronous ($s = -20\%$) and sub-synchronous ($s = 20\%$) operation of the DFIG.

simulations of the test system in the PSCAD/EMTDC environment and processing of the waveforms in the MATLAB environment. The test system parameters are provided in Table 3.1.

A balanced fault occurs at 40% of line jk at $t = 2$ s with $R_f = 1$ Ω. Figure 3.2 shows the phase-A fault currents measured at Rij during the sub-synchronous ($s = 20\%$) and super-synchronous ($s = -20\%$) operation of the DFIG. After the onset of the fault, the fault current increases immediately and then decreases gradually to a steady state value. The damping speed depends on the rotor and crowbar resistances. Figure 3.2 also demonstrates that the fault current frequency depends on the generator slip. Figure 3.3 shows the voltage at the relay location during sub-synchronous and super-synchronous operation of the DFIG. Figure 3.3 shows that there is a significant drop in voltage after the fault. The voltage will not drop to zero because of the impedance between the relay and the fault location.

The frequency spectrum of instantaneous voltages and currents are shown in Figures 3.4 and 3.5, where the voltage and current spectrums are obtained by applying the fast fourier transform (FFT) to the first 200 ms of the fault current waveforms. Figure 3.4 shows that the largest peak of the current and voltage spectrums during the sub-synchronous operation of the DFIG are at around 43 Hz and 60 Hz, respectively. During the super-synchronous operation of the DFIG, the highest peak of the current and voltage spectrums are at around

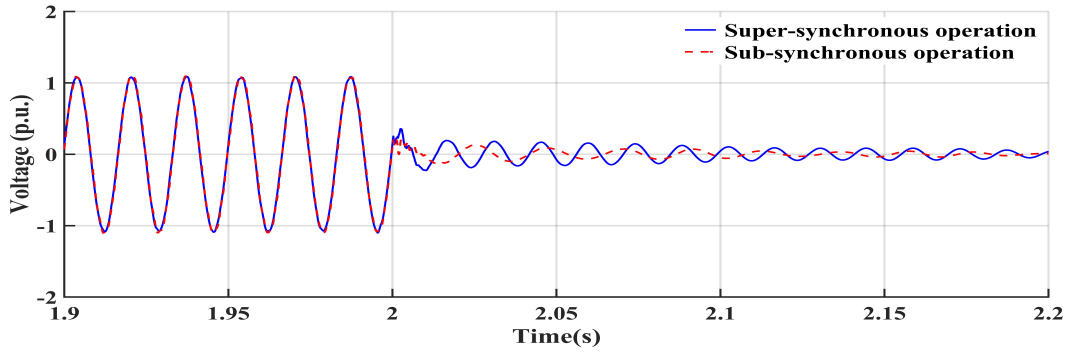

Figure 3.3: Phase-A voltage of the WF measured at Rij after a balanced fault on line jk for super-synchronous ($s = -20\%$) and sub-synchronous ($s = 20\%$) operation of the DFIG.

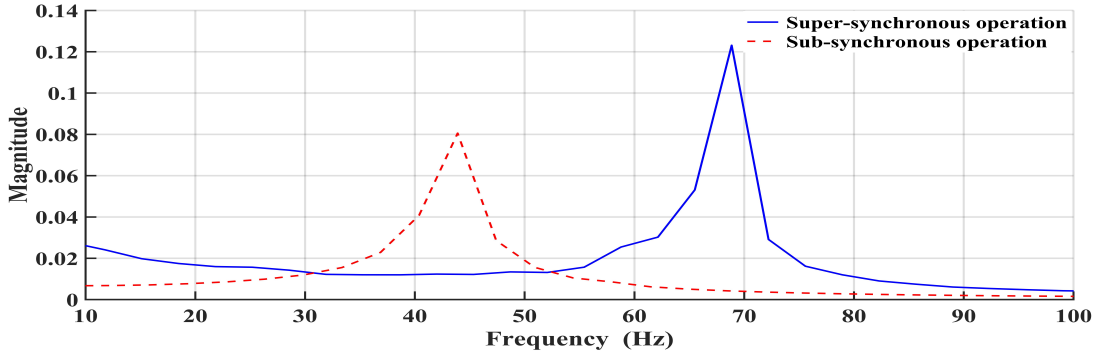

Figure 3.4: Frequency spectrum of phase-A current measured at Rij after a balanced fault on line jk for super-synchronous ($s = -20\%$) and sub-synchronous ($s = 20\%$) operation of the DFIG.

69 Hz and 60 Hz, respectively, as shown in Figure 3.5. Therefore, the frequency of the voltage and current at the relay location are different from each other for both sub- and super-synchronous operations of the DFIG.

To illustrate the negative effect of the off-nominal frequency of the fault current on the performance of Rij, the impedance trajectory measured by Rij after a fault at 40% of line jk is presented in Figure 3.6. The impedance trajectory after the balanced fault is

Table 3.1: Parameters of the test system.

Component	Parameter	Value
DFIG	Apparent power	5 MVA
	Nominal voltage	690 V
	Stator resistance	0.0054 p.u.
	Rotor resistance	0.00607 p.u.
	Magnetizing inductance	4.5 p.u.
	Stator inductance	0.1 p.u.
	Rotor inductance	0.11 p.u.
	DC link rated voltage	1200 V
	DC link capacitor size	2 mF
Source	Nominal voltage	132 kV
	Positive- and negative-sequence impedances	$1\angle 80°$ p.u.
	Zero-sequence impedance	$1.5\angle 80°$ p.u.
DFIG transformer	Apparent power	5.5 MVA
	Nominal voltage	690 V/900 V/33 kV $YgYgYg$
	Positive-sequence leakage reactance (1-2)	0.08 p.u.
	Positive-sequence leakage reactance (1-3)	0.06 p.u.
	Positive-sequence leakage reactance (2-3)	0.05 p.u.
Main transformer	Apparent power	50 MVA
	Nominal voltage	33 kV/132 kV ΔYg
	Positive-sequence leakage reactance	0.025 p.u.
Transmission line	Positive- and negative-sequence impedances	$0.144\angle 86°$ Ω/km
	Zero-sequence impedance	$0.437\angle 86°$ Ω/km

changing drastically.

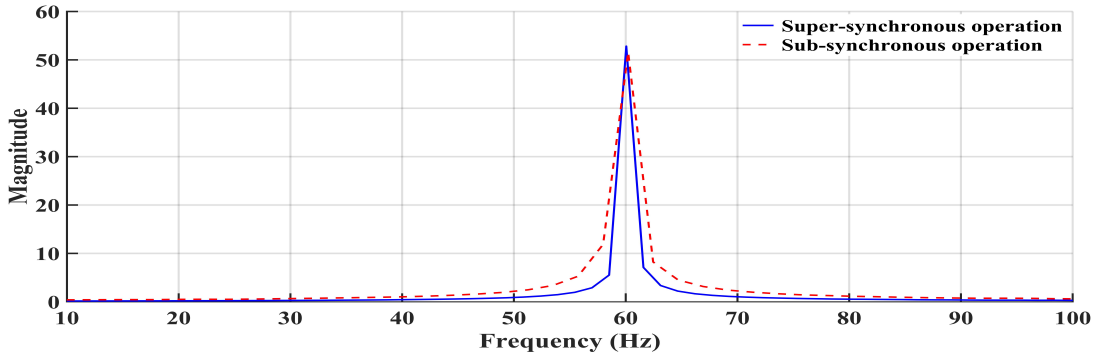

Figure 3.5: Frequency spectrum of phase-A voltage measured at Rij after a balanced fault on line jk for super-synchronous ($s = -20\%$) and sub-synchronous ($s = 20\%$) operation of the DFIG.

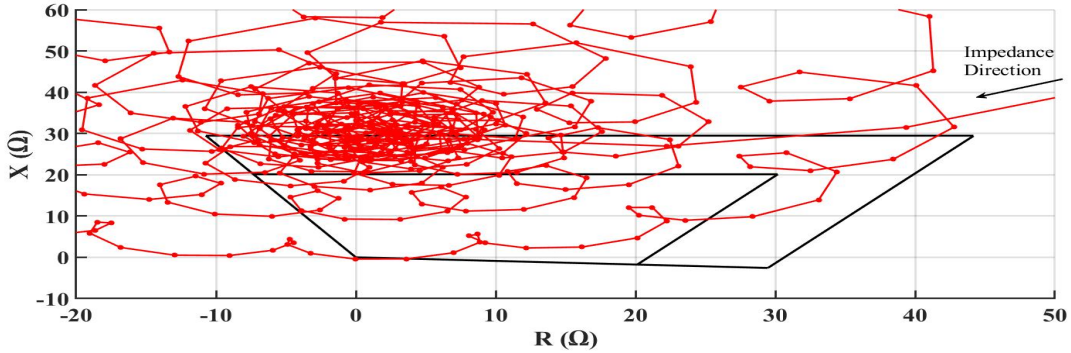

Figure 3.6: Impedance trajectory measured by the AG element of relay Rij after a balanced fault at 40% of line jk with $R_f = 1\ \Omega$ for super-synchronous ($s = -20\%$) operation of the DFIG.

3.2.2 Unbalanced Faults

The distance relay at the terminal of the DFIG-based WF might be facing the same problem as that of a balanced fault when a severe unbalanced fault occurs close to the DFIG. The approximate fault current injected by a DFIG-based WF for different types of faults is calculated as follows [23]

$$i_s(t) = i_{sf}(t) + i_{sn}(t) \ , \tag{3.6}$$

$$i_{sf}(t) = (\frac{V_1}{j\omega_s L'_s} - k_r \frac{\psi_{rf,1}}{L'_s})e^{j\omega_s t} + \frac{V_2}{Z_2}e^{-j\omega_s t} \ , \tag{3.7}$$

$$i_{sn}(t) = \frac{V_{pre} - (V_1 - V_2)}{j\omega_s L'_s}e^{-\frac{t}{T_s}} - \frac{k_r}{L'_s}(de^{-\frac{t}{T_s}} + ce^{-\frac{t}{T_r}}e^{j\omega_r t})(\psi_{r,pre} - (\psi_{rf,1} + L_{r2}\frac{V_2}{Z_2})) \ , \tag{3.8}$$

where V_{pre} is the pre-fault voltage, V_1 and V_2 are the positive- and negative-sequence voltages, respectively, and ω_r is the rotor angular frequency. $\psi_{r,pre}$ and $\psi_{rf,1}$ are the pre-fault rotor flux and the magnitude of the positive-sequence forced component of the post-fault rotor flux, respectively. Also, T_s and T_r are the stator and rotor time constants, respectively. According to (3.6)-(3.8), the fault current of the DFIG-based WF consists of a decaying dc component, a decaying ac component at the rotor frequency, and an ac component at the synchronous frequency. The fault current is calculated by assuming the activation of the crowbar circuit due to the large negative-sequence current passing through the back-to-back converter for an unbalanced fault. When a severe unbalanced fault occurs close to the terminal of the DFIG-based WF, the voltage drops significantly and the positive- and negative-sequence components of the voltage will be small. By considering the insignificant changes of the other coefficients of the fault current equation based on the equations presented in [23], the magnitude of the ac component at the synchronous frequency decreases while there will be an increase in the magnitude of the decaying dc component and the decaying ac component at the rotor frequency. Therefore, the effect of rotor frequency on the frequency of the fault current will be considerable. However, by moving the fault location away from the DFIG-based WF, the voltage sag will reduce; therefore, the ac component at the synchronous frequency will be the main component of the fault current.

Figure 3.7 illustrates the frequency spectrum of the fault current measured by Rij for different unbalanced faults at the beginning of line ij when the DFIG is operating at $s = -30\%$. The main peak of the current spectrum is at 60 Hz and another peak with a smaller magnitude is around 78 Hz (the rotor frequency). Among different types

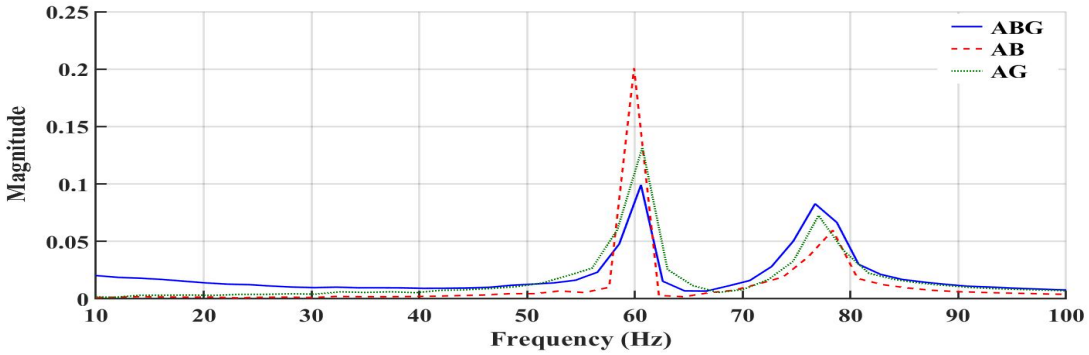

Figure 3.7: Frequency spectrum of phase-A current measured at Rij for different unbalanced faults at the beginning of line ij for super-synchronous ($s = -30\%$) operation of the DFIG.

of unbalanced faults, the ABG fault has the largest peak of the current spectrum at the rotor frequency, resulting in the most negative impact on the performance of Rij. Figure 3.8 depicts the frequency spectrum of the fault current measured by Rij for different unbalanced faults at the beginning of line jk when the DFIG is operating at $s = -30\%$. Compared to Figure 3.7, the magnitude of the main peak at 60 Hz increases, while the magnitude of another peak at around the rotor frequency has decreased.

The impedance trajectories measured by Rij for an ABG fault at two different locations are shown in Figure 3.9. For the fault at the beginning of line ij, the impedance trajectory correctly enters zone 1; but, there is a small fluctuation in the impedance trajectory due to the large current components with rotor frequency in the fault current measured by Rij. However, this fluctuation does not affect the operation of Rij as the fault has occurred in zone 1. Even if the fluctuation in the impedance trajectory is significant, Rij still operates properly as the fault is an internal fault. For the fault at the beginning of line jk, the impedance trajectory correctly enters zone 2 and remains within zone 2 despite an insignificant fluctuation in the impedance trajectory due to the small current component with the rotor frequency. Therefore, the distance relay Rij operates properly as a backup for line jk. Since unbalanced faults affect the frequency of the DFIG fault current, they are also considered in the new relaying algorithm developed in the next section.

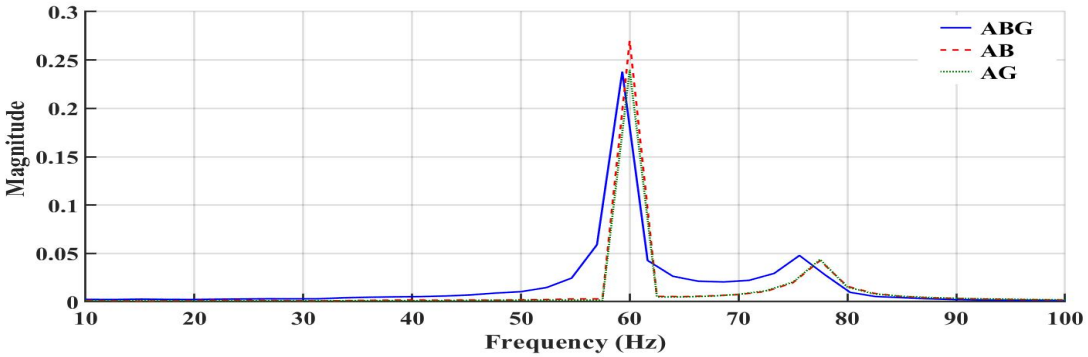

Figure 3.8: Frequency spectrum of phase-A current measured at Rij for different unbalanced faults at the beginning of line jk for super-synchronous ($s = -30\%$) operation of the DFIG.

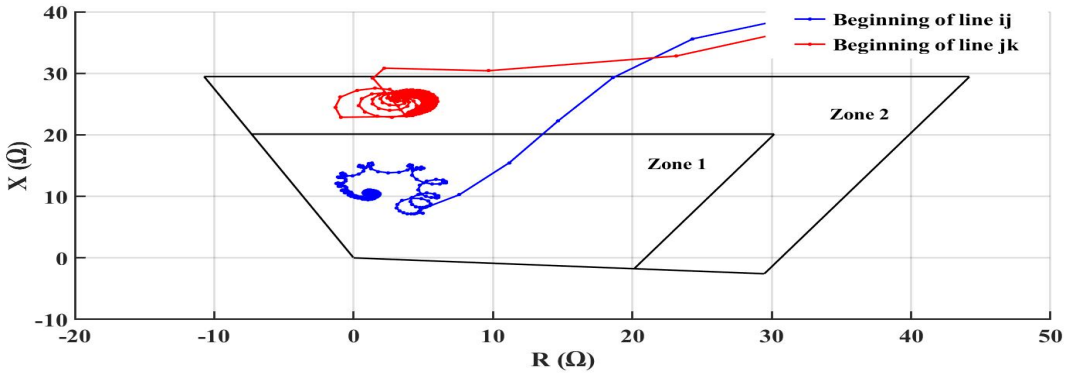

Figure 3.9: Impedance trajectory measured by the AG element of relay Rij after an ABG fault at the beginning of lines ij and jk for super-synchronous ($s = -30\%$) operation of the DFIG.

3.3 Modified Distance Element Type II

Distance relays are not able to provide instantaneous protection for 100% of the length of the transmission line due to overreaching and underreaching issues. In order to protect the entire length of the transmission line, a communication link along with the distance relays at the two ends of the transmission line is used. In many communication-based

(pilot) protection schemes, the communication link is used to communicate signals such as current and voltage measurements and frequency from one side to the other side of the line [32]. The communication of large amount of information requires high communication bandwidth.

In this section, a new pilot protection scheme with low bandwidth requirements for protecting the line connected to a DFIG-based WF is presented to address the previously-discussed protection challenge arising from the off-nominal frequency of the fault current. The new relaying algorithm called modified distance element type II relies on the communication of a binary signal from one side to the other side of the line in case of a fault on the transmission line. The binary signal is associated with the frequency of the fault current captured by the relay at the remote end of the transmission line connected to the DFIG-based WF.

Figure 3.10 depicts the decision-making process of the relay Rij at the DFIG terminal when the system is subjected to a short-circuit fault. The modified distance element type II is based on the frequency tracking of the fault currents injected by the DFIG-based WF and the ac grid to the line. The modified distance element type II has two main components which are described in the rest of this section.

3.3.1 Fault Detection

The first step in this protection scheme is to distinguish the fault condition from the power system disturbances such as power swings and load encroachments. In this protection scheme, the fault detection algorithm presented in [33] is used. The fault detection algorithm of [33] is based on the asymmetry of the instantaneous fault current waveform after the onset of the fault. This phenomenon is not observed during the normal operation of the power system (even during power swings and load encroachments). In this algorithm, the one-cycle moving sum of the current samples is calculated. Because of the symmetric nature of the current waveform during normal operation of the power system, the moving sum of the samples becomes around zero. On the other hand, the moving sum of the samples deviates from zero in case of faults due to th large dc component of the fault current waveform [33].

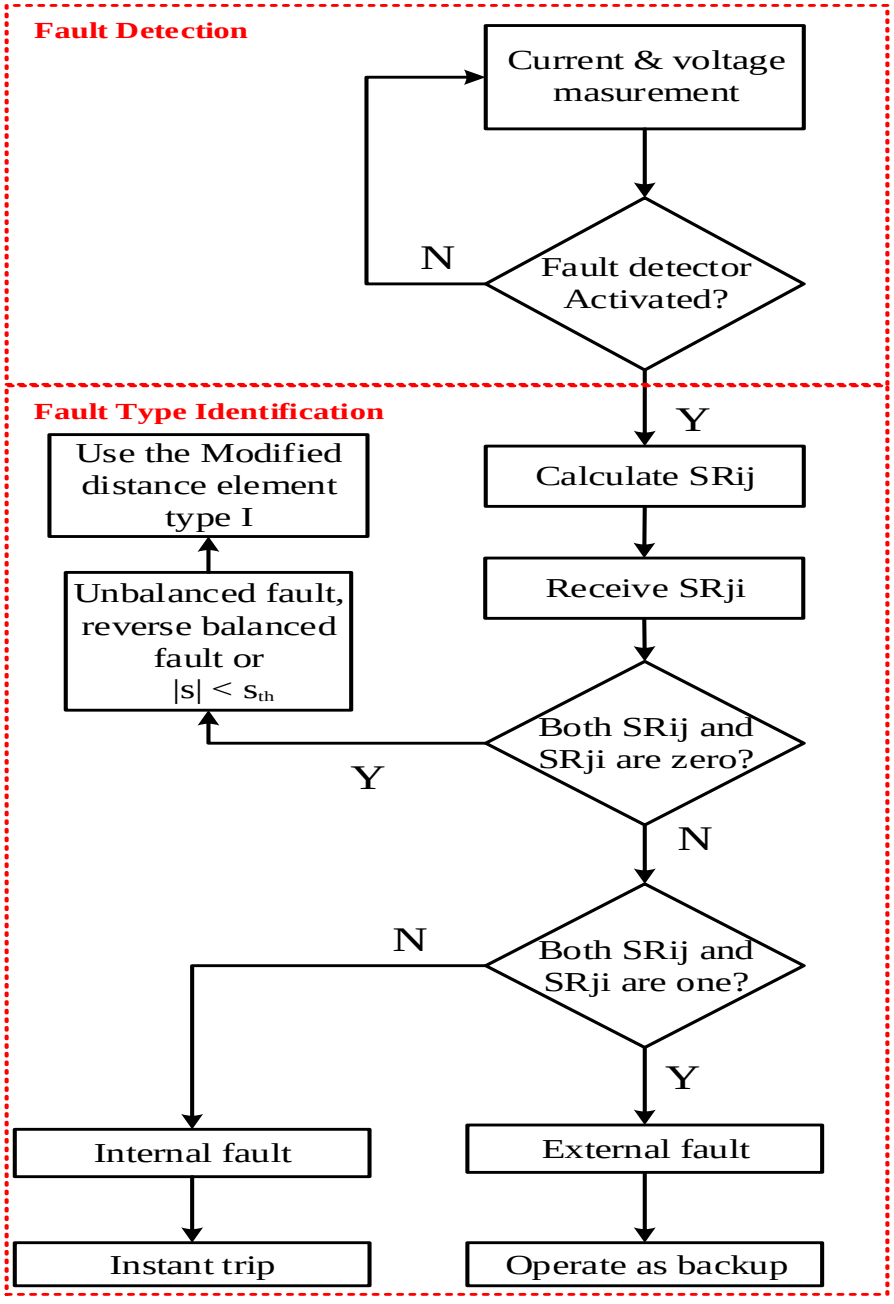

Figure 3.10: Modified distance element type II for the operation of Rij.

3.3.2 Fault Type Identification

The slip of a DFIG can change in the range of ±30% and this affects the frequency of the fault current measured by the relay. When the generator slip is near zero, the frequency of the fault current is close to the nominal frequency. Therefore, the frequency of voltage and current are almost the same and the conventional distance relay works properly. However, during DFIG operation at a non-zero slip, the frequency of the fault current deviates from the nominal frequency, resulting in the maloperation of conventional distance relays.

To overcome this issue, the difference between the frequency of the fault current injected by the DFIG-based WF and the ac grid to the fault location is used to detect the fault. Based on (3.4), during a fault, the ac grid injects a fault current with the nominal frequency to the fault location regardless of the slip value of the DFIG. In contrast, the frequency of the fault current injected by the DFIG-based WF depends on the machine slip and it changes in the range of 42-78 Hz in a 60 Hz system. Therefore, by knowing the frequency of the fault current at the relays located at two ends of the transmission line, internal faults can be detected.

When the DFIG operates with a slip close to zero, the fault current frequency of the DFIG-based WF is very close to the nominal frequency. Hence, both fault current and voltage have almost the same frequency, resulting in the correct calculation of the impedance by Rij. However, by increasing or decreasing the slip, the fault current frequency of the DFIG-based WF deviates more from the nominal frequency. As a result, there will be drastic changes in the impedance trajectory calculated by Rij. Therefore, a suitable threshold for the slip can be defined to determine whether the fault current frequency is within a pre-defined bound, i.e., relatively close to the voltage frequency.

$$-s_{th} \leq s \leq s_{th} \ , \tag{3.9}$$

$$f_{lb} \leq f \leq f_{ub} \ , \tag{3.10}$$

$$f_{lb} = (1 - s_{th}) f_s \ , \tag{3.11}$$

$$f_{ub} = (1 + s_{th}) f_s \ , \tag{3.12}$$

where s_{th} is the slip threshold, f is the fault current frequency, and f_{lb} and f_{ub} are the lower and upper bounds of the frequency, respectively. The threshold value is set based on the fault response of the test system.

Two binary variables, $SRij$ and $SRji$, are defined based on the frequency of the fault current measured at Rij and Rji. When the fault current frequency measured at Rij is within the range defined in (3.10), $SRij$ would be set to zero, while it will become one if the fault current frequency is out of the range defined in (3.10). There is a similar expression for $SRji$ based on the fault current frequency measured at the relay at the remote end of the line. $SRij$ ($SRji$) signal is sent to the other side of the line via the communication link to make a decision regarding the location of the fault. Figure 3.11 shows the direction of the fault currents as well as $SRij$ and $SRji$ values after the occurrence of a fault at three different locations.

After a fault, three scenarios may occur;

1. $\boldsymbol{SRij = SRji = 0}$
   In this scenario, the fault current frequency measured at $\boldsymbol{Rij}$ and $\boldsymbol{Rji}$ is within the range defined in (3.10). This scenario will happen if

   (a) A reverse fault occurs behind relay $\boldsymbol{Rij}$ regardless of the DFIG's slip and the fault type, or

   (b) the current frequency measured at $\boldsymbol{Rij}$ and $\boldsymbol{Rji}$ is within the range defined in (3.10), regardless of the fault location.

   In the case of a reverse fault, the fault currents measured by both relays are injected by the ac grid and therefore the current frequency is 60 Hz. Furthermore, regardless of the fault location, if the fault current frequency measured at both relays is close to 60 Hz, $\boldsymbol{SRij = SRji = 0}$. Therefore, in this scenario, since the fault current frequency calculated by both relays are within the range of (3.10), the impact of

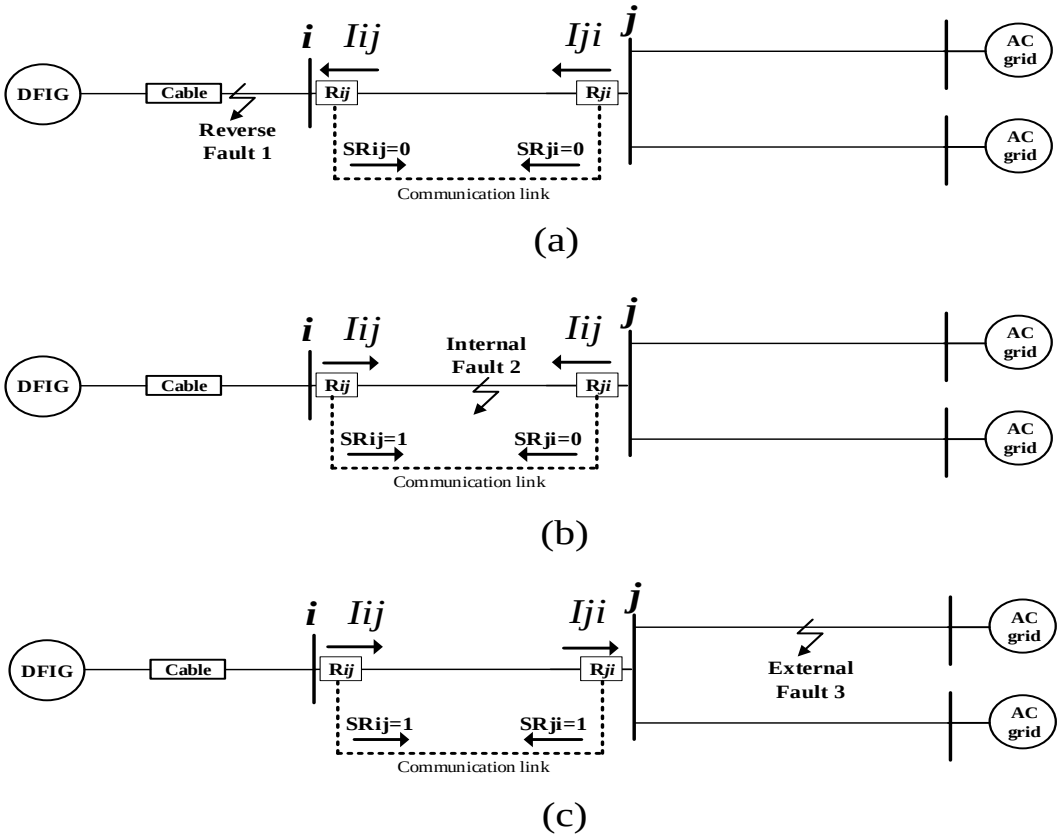

Figure 3.11: $SRij$ and $SRji$ signals after the occurrence of a balanced (a) reverse fault, (b) internal fault, and (c) external fault.

DFIG-based WF on the operation of $\boldsymbol{Rij}$ and $\boldsymbol{Rji}$ will be the same as the fixed-speed SCIG-based WF. Thus, the modified distance element type I presented in Section 2 can be used for protecting the line connected to the DFIG-based WF.

2. $\boldsymbol{SRij = 1}$ & $\boldsymbol{SRji = 0}$

   In this scenario, the current frequency measured at $\boldsymbol{Rij}$ is out of the range defined in (3.10). This scenario happens when an internal balanced fault occurs on the transmission line and the generator slip is out of the range defined in (3.9). Also,

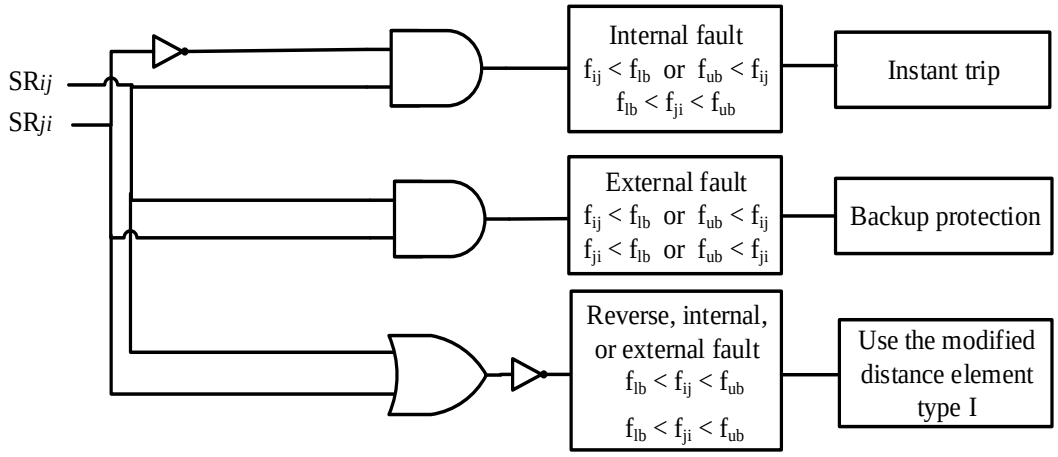

Figure 3.12: Logic diagram for fault type identification implemented at Rij.

this scenario might happen when a severe unbalanced fault occurs close to the DFIG terminal and the generator slip is not within the range defined in (3.9). In this scenario, an internal fault has occurred and the relays located at two ends of the line must operate instantaneously.

3. $\boldsymbol{SRij = SRji = 1}$
   In this scenario, the fault currents measured at relays are injected by the DFIG-based WF and the generator is operating with a slip out of the range defined in (3.9). Therefore, the fault current frequency at both relay locations is out of the range defined in (3.10). In this scenario, an external fault has occurred and the relay at the terminal of DFIG-based WF should only provide backup protection.

3.4 Simulation Results

To investigate the performance of the modified distance element type II, the protection scheme is implemented in the test system shown in Figure 3.1. The test system is studied

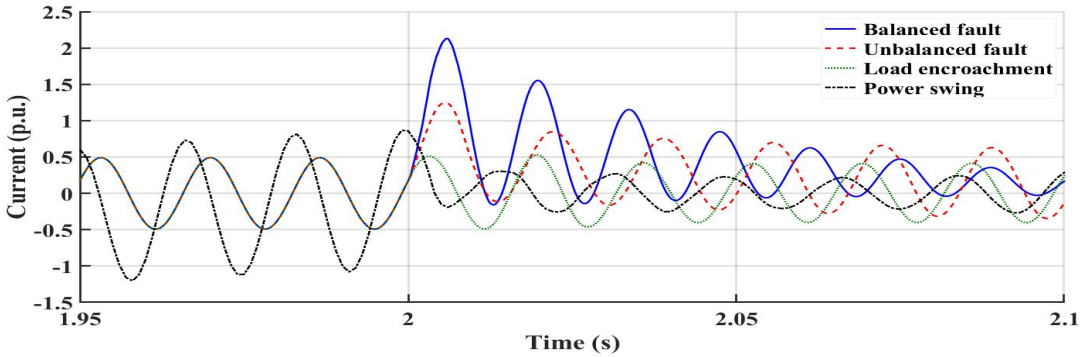

Figure 3.13: Phase-A current under a balanced fault, an unbalanced fault, a load encroachment, and a power swing condition.

under three conditions including short-circuit faults, power swings, and load encroachments. Two fault scenarios, a balanced fault and an AG fault at the end of line ij at $t = 2\ s$ with $Rf = 1\ \Omega$, are considered. To create a power swing condition in the system, a transmission line parallel with line ij and with similar characteristics is added to the system. Then, a balanced fault at the middle of the new line is initiated at $t = 1.9\ s$ and is removed at $t = 2\ s$ by opening the circuit breakers located at the two sides of the new line. For simulating the load encroachment condition, a new load (100 MW and 25 MVAR) is connected to bus j at $t = 2\ s$.

The phase-A current for the four scenarios are shown in Figure 3.13. Figure 3.13 shows that the current waveforms associated with the power swing and load encroachment are almost symmetrical about the x-axis; however, the current waveforms associated with the balanced and unbalanced faults are asymmetrical about the x-axis due to the existence of the decaying dc component in the waveform. According to Figure 3.14 which illustrates the moving sum over one cycle of the waveforms shown in Figure 3.13, the value of the moving sum over one cycle is significant for balanced and unbalanced faults while it can be neglected for power swing and load encroachment scenarios. The reason for the unsymmetrical waveform of the power swing scenario before $t = 2\ s$ is the existence of a fault on the new line for creating the power swing after $t = 2\ s$.

To investigate the performance of the second component of the modified distance el-

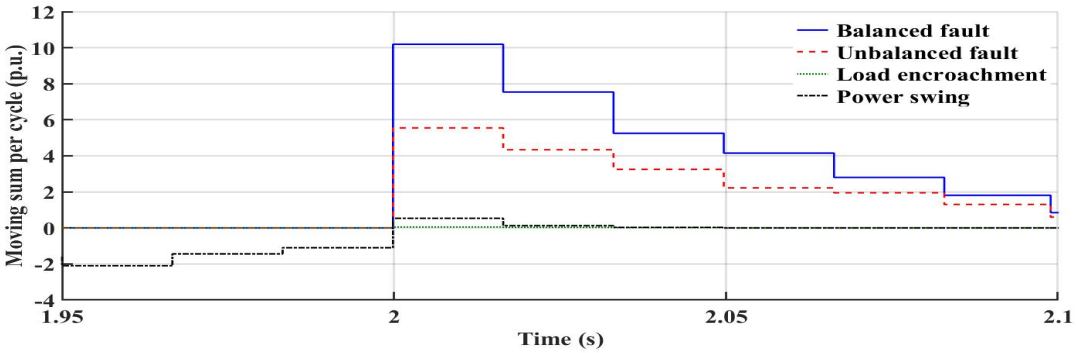

Figure 3.14: The moving sum over one cycle under a balanced fault, an unbalanced fault, a load encroachment, and a power swing condition.

ement type II, first, the slip range of (3.9) is identified. Based on the range, the proper relaying algorithm is selected between the modified distance elements types I and II. When the DFIG operates at a small slip value, the fault current of the DFIG is dominated by the ac component at the synchronous frequency [23], [35]. Therefore, the frequency of the fault current will be very close to the nominal frequency, resulting in the reliable operation of the modified distance element type I. The upper bound of the slip range corresponds to the maximum slip value associated with the reliable operation of the modified distance element type I. In other words, when the DFIG operates at any slip value lower than the upper bound, the impedance trajectory associated with a balanced fault in zone 2 of Rij will remain in zone 2 for sufficient time such that the modified distance element type I can reliably detect the fault.

On the other hand, the upper bound of the slip range should be selected to be large enough so that there is enough frequency deviation in the fault current for the reliable operation of the modified distance element type II. In other words, when the DFIG operates at any slip value higher than the upper bound, the proper values are assigned to $SRij$ and $SRji$ such that the modified distance element type II can reliably identify the type of the fault, i.e. reverse, internal, or external. Figure 3.15 illustrates the fault current frequency associated with three different faults when the DFIG operates at $s = -3\%$: a balanced reverse fault at the DFIG terminal, a balanced internal fault at the end of line ij, and a

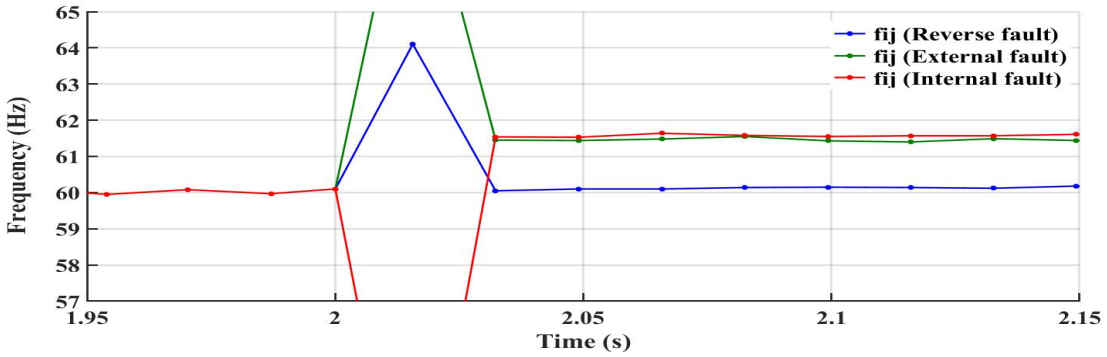

Figure 3.15: Frequency of I_{ij} for three fault scenarios ($s = -3\%$).

balanced external fault at 50% of line jk. The selected faults occur at the end of each zone, results in the smallest magnitude of the current component with the off-nominal frequency compared to other faults in that zone. According to Figure 3.15, the difference between the fault current frequency associated with these faults is about 1.3 Hz, which results in enough frequency deviation of the fault current for reliable operation of the modified distance element type II. Therefore, $s_{th} = 3\%$ is selected as the upper bound, i.e. the threshold value, of the slip range to ensure the modified distance elements types I and II have a reliable performance during a fault ($f_{ub} = 61.8$ Hz and $f_{lb} = 58.2$ Hz).

To ensure the modified distance element type I can reliably identify all balanced faults in zone 2, the shortest time period for which the impedance trajectory remains in zone 2 for an uncleared balanced fault is determined. As the DFIG operates in both super- and sub-synchronous speeds, the critical scenarios for each operating mode should be selected and among them, the shorter time period for which the impedance trajectory remains in zone 2 is used to select the relay threshold K. Therefore, the slip range selected for the operation of the modified distance element type I is divided into two parts, $-s_{th} \leq s \leq 0$ and $0 \leq s \leq s_{th}$.

For both operating modes of the DFIG, the critical fault scenario is associated with a balanced fault at the end of zone 2 (50% of the largest adjacent line). This scenario is selected as the critical scenario because it is associated with the smallest fault current. As explained in Chapter 2, a smaller fault current results in a larger Z_{error}^{ext} in (2.4) and conse-

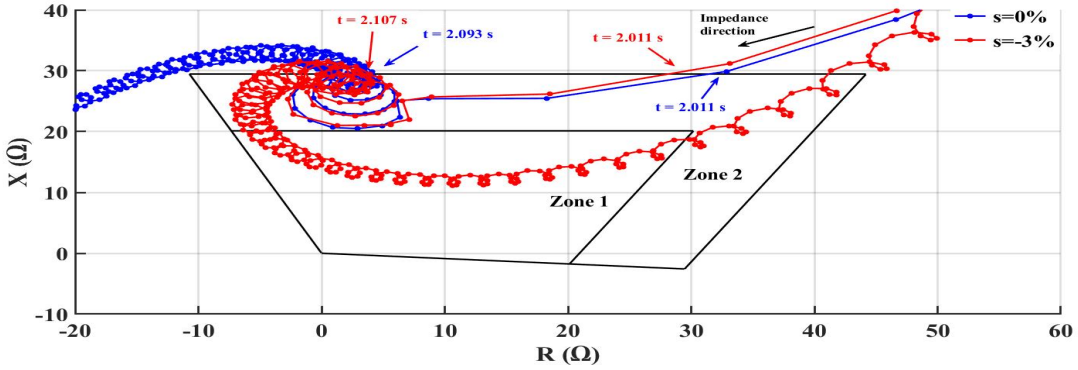

Figure 3.16: Impedance trajectories calculated by Rij for a balanced external fault at 50% of the line jk for $s = -3\%$ and $s = 0\%$.

quently, faster departure of the impedance trajectory from zone 2 in the R-X diagram. The fault current is also inversely proportional to $(1 - s)$. Therefore, for the super-synchronous mode of the generator at $s = -3\%$, the fault current will have a smaller value and consequently, the impedance trajectory will immediately leave zone 2 in the R-X diagram. Also, for the sub-synchronous mode of the generator at $s = 0\%$, the fault current will have a small magnitude resulting in the fast departure of the impedance trajectory from zone 2.

Figure 3.16 illustrates the impedance trajectories associated with these two critical fault scenarios that are measured by Rij. During the super-synchronous operation of the generator, the impedance trajectory enters zone 2 and remains within zone 2 for $\Delta T_{R2} = 96\ ms$ and then incorrectly enters zone 1. For the sub-synchronous operation of the generator, on the other hand, the impedance trajectory enters zone 2 and remains within zone 2 for $\Delta T_{R2} = 82\ ms$ and then leaves the relay zones. Therefore, $K = 82\ ms$ is selected for distance element type I.

To evaluate the performance of the fault type identification component, four fault conditions are studied:

• **Balanced reverse fault**

As the fault current at the two ends of line ij is injected by the ac grid, the slip value of the DFIG does not affect the frequency of currents measured at Rij and Rji; therefore, this scenario can be evaluated for any generator slip value. A balanced reverse fault on the terminal of the DFIG-based WF with $R_f = 1\ \Omega$ is studied when the generator is operating at $s = -20\%$. The phase-A fault current measured at Rij and Rji are depicted in Figure 3.17. Figure 3.17 shows that the fault current magnitudes have a significant increase after the onset of the fault and they reach around 18 p.u. The current waveforms consist of a dc component during the fault, but no substantial damping is observed as the currents measured at both relays are injected by the ac grid. The fault current frequency observed by both relays remains near 60 Hz, Figure 3.18, resulting in $SRij = SRji = 0$. In this fault condition, a conventional distance element can be used for the fault detection. According to Figure 3.18, the first frequency sample calculated right after the fault is not a good representation of the current frequency during the fault as it is based on one-cycle of the current measurement, where the first half-cycle corresponds to the pre-fault period and the second half-cycle is associated with the fault duration. Therefore, $SRij$ ($SRji$) signal becomes one only if the measured frequency is out of the pre-defined range of (3.10) for more than one sample. The impedance trajectory calculated by Rij is shown in Figure 3.19. The impedance trajectory lies in the third quadrant of the R-X diagram without incorrectly entering zones 1 and 2 of the distance relay.

• **Balanced internal fault for the generator operation at low slip values**

For this fault condition, a balanced fault at the end of line ij is studied when the generator is operating at $s = -3\%$ as this is associated with the maximum deviation of the fault current frequency from the ac grid frequency as well as the lowest current value for $\mid s \mid \leq s_{th}$ based on (2.4). In this fault condition, the fault current measured at Rij is injected by the DFIG-based WF, while the fault current measured by Rji comes from the ac grid. According to Figure 3.20 that depicts phase-A current measured at Rij and Rji, there is a significant damping in the fault current of I_{ij}. Figure 3.21 shows the frequency of the fault currents I_{ij} and I_{ji}. The frequency of both I_{ij} and I_{ji} remains within the pre-defined

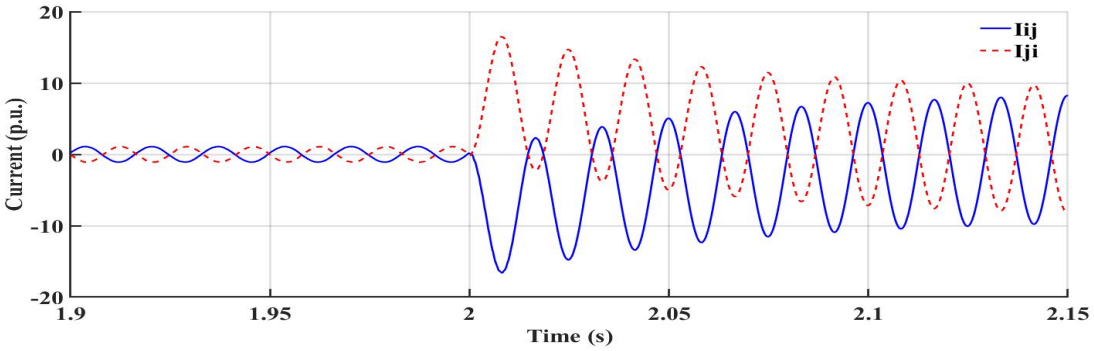

Figure 3.17: Fault currents measured at Rij and Rji for a balanced reverse fault ($s = -20\%$) at the terminal of the DFIG-based WF.

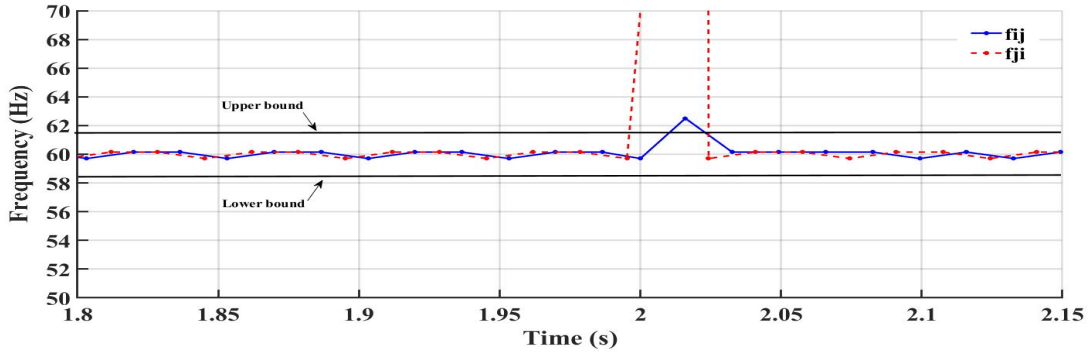

Figure 3.18: Frequency of I_{ij} and I_{ji} for a balanced reverse fault ($s = -20\%$) at the terminal of the DFIG-based WF.

frequency bounds and only leaves the bounds for one sample; therefore $SRij = SRji = 0$. Hence, the modified distance element type I, presented in Chapter 2 for fixed-speed SCIG-based WF, can be used to detect the fault. The impedance trajectory calculated by Rij is depicted in Figure 3.22. The impedance trajectory correctly enters zone 2 and remains within zone 2 for 158 ms, and then incorrectly enters zone 1. Since the impedance trajectory remains in zone 2 for more than $k = 74\ ms$, the fault current waveform will be tracked to provide the proper coordination between Rij and downstream relays (Rjk and Rjl). Based on Figure 3.20, the current waveform of Rij keeps damping for more than 300 ms

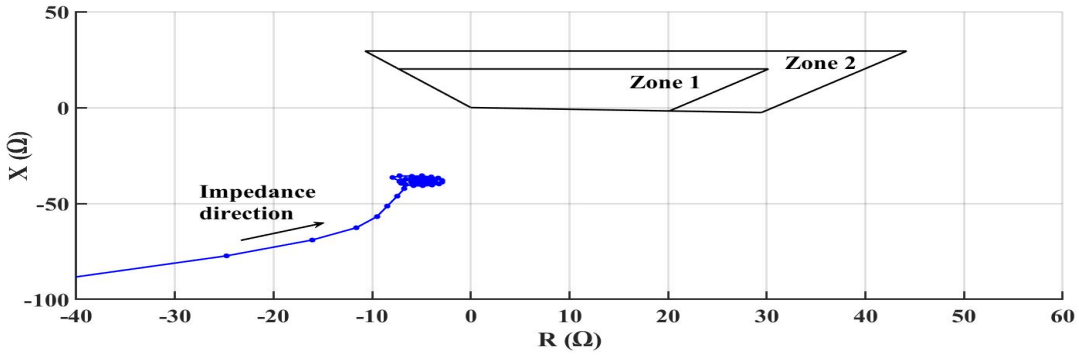

Figure 3.19: Impedance trajectory calculated by Rij for a balanced reverse fault ($s = -20\%$) at the terminal of the DFIG-based WF.

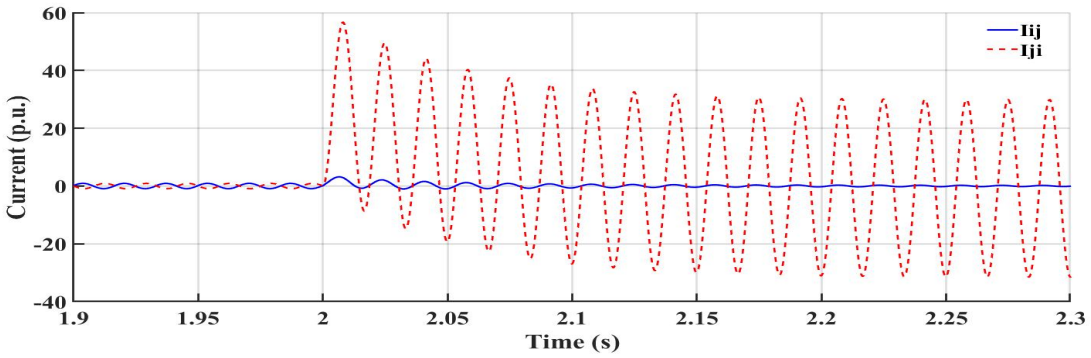

Figure 3.20: Fault currents measured at Rij and Rji for a balanced fault at the end of line ij ($s = -3\%$).

(the time delay setting for the backup zone), resulting in the proper operation of Rij after this time delay.

- **Balanced internal fault for the generator operation at high slip values**

In this fault condition, an internal fault at the end of line ij is studied when the generator is operating at $s = -30\%$. This fault condition is the one which results in the maximum fault current frequency deviation as well as the lowest fault current value. Figure 3.23

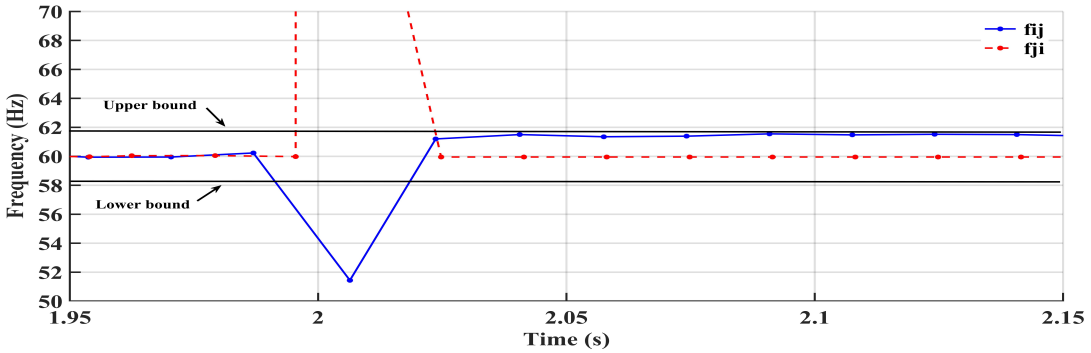

Figure 3.21: Frequency of I_{ij} and I_{ji} for a fault at the end of the line ij ($s = -3\%$).

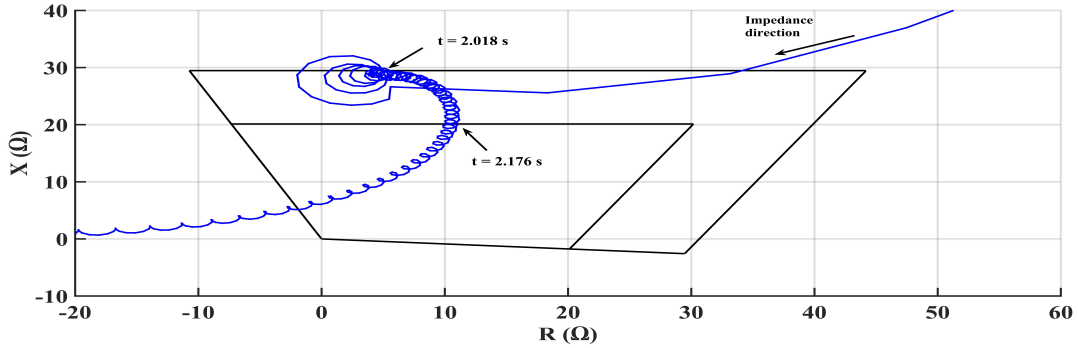

Figure 3.22: Impedance trajectory calculated by Rij for a balanced fault at the end of the line ij ($s = -3\%$).

illustrates the inability of the conventional distance relay to measure the correct impedance from the relay location to the fault location due to the off-nominal frequency of the fault current injected by the DFIG-based WF. Figure 3.24 depicts the frequency of fault current waveforms at the two ends of line ij. According to Figure 3.24, the frequency of the fault current measured at Rij deviates significantly from the nominal frequency and is out of the frequency bounds ($f_{lb} \leq f_{ij} \leq f_{ub}$) for more than one sample, while the fault current frequency at Rji remains within the frequency bounds. Therefore, $SRij = 1$ and $SRji = 0$, which results in correct identification of the internal fault by Rij and Rji.

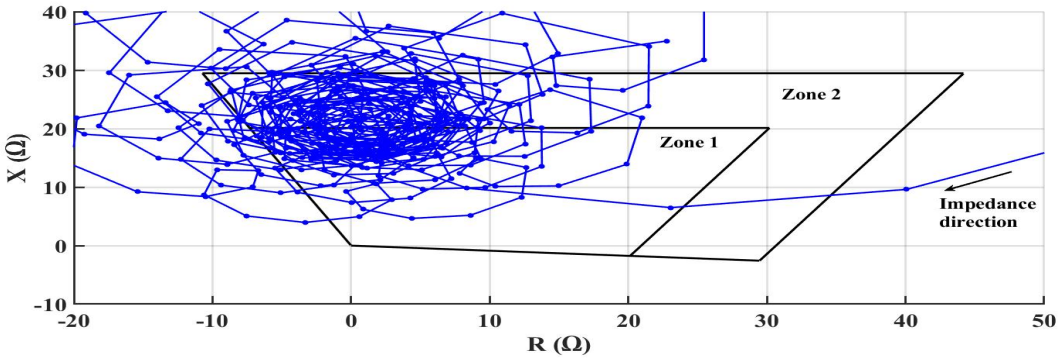

Figure 3.23: Impedance trajectory calculated by Rij for a balanced internal fault at the end of line ij ($s = -30\%$).

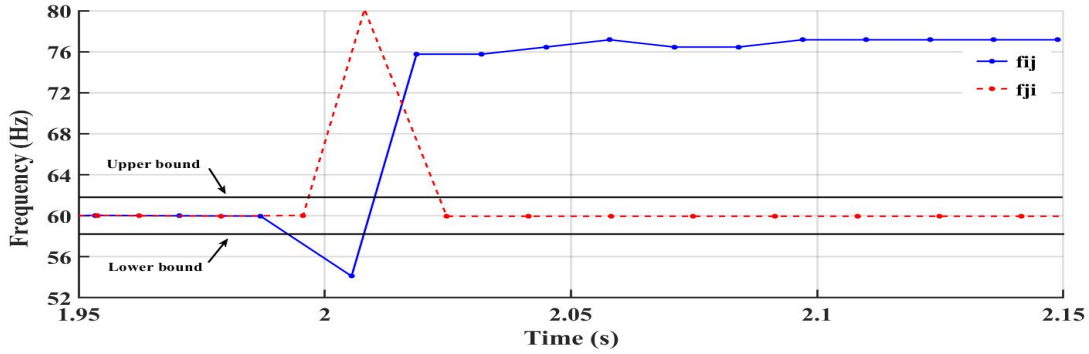

Figure 3.24: Frequency of I_{ij} and I_{ji} for a balanced internal fault at the end of line ij ($s = -30\%$).

• **Balanced external fault in zone 2 of** Rij

In this fault condition, a balanced fault at 50% of line jk is studied when the generator operates at $s = -30\%$ in which the fault current measured by Rij has the maximum frequency deviation and the lowest value for an external fault in zone 2 of Rij. The impedance trajectory is shown in Figure 3.25. Although this is an external fault in zone 2 of Rij, the impedance trajectory enters zone 1 and therefore, a conventional distance relay fails to identify the fault in the second zone correctly and loses the coordination with relay

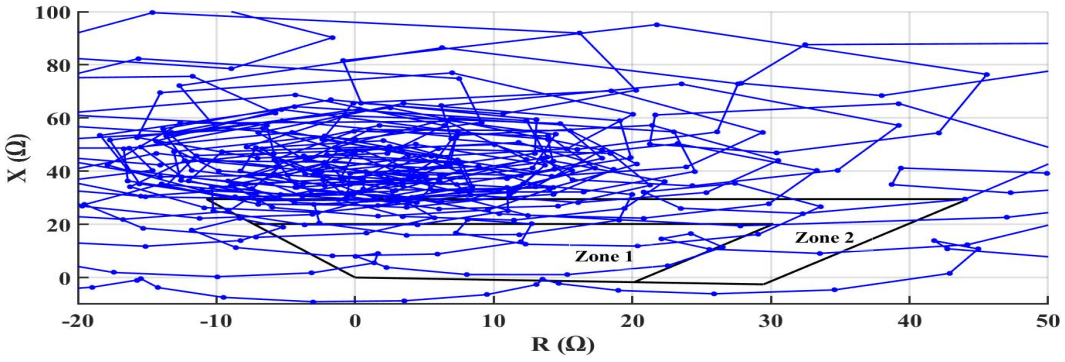

Figure 3.25: Impedance trajectory calculated by Rij for a balanced external fault at 50% of line jk ($s = -30\%$).

Rjk. In this fault condition, the frequency of the fault current waveforms, shown in Figure 3.26, deviates from the nominal frequency and is out of the frequency bounds. Therefore, $SRij = SRji = 1$, and the fault is correctly identified as an external fault.

- **Unbalanced external fault**

In this fault condition, an ABG fault at the beginning of line ij is studied when the generator operates at $s = -30\%$. The frequency of the fault currents I_{ij} and I_{ji} are depicted in Figure 3.27. The frequency of both I_{ij} and I_{ji} remains within the pre-defined frequency bounds and only leaves the bounds for one sample after the fault; therefore $SRij = SRji = 0$. Hence, the modified distance element type I is used to detect the fault. The impedance trajectory measured by Rij for this fault condition is already illustrated in Figure 3.9. The impedance trajectory correctly enters zone 2 and remains within zone 2. Therefore, the relay at the terminal of the DFIG can be correctly operated as a backup for the downstream relays.

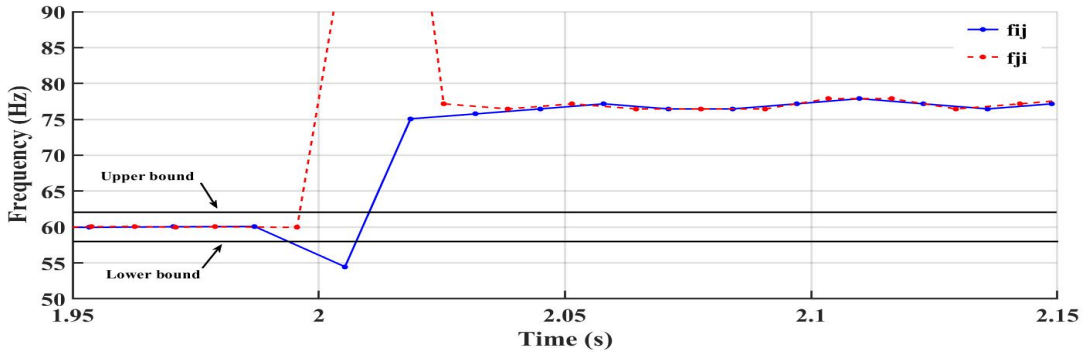

Figure 3.26: Frequency of I_{ij} and I_{ji} for a balanced external fault at 50% of line jk ($s = -30\%$).

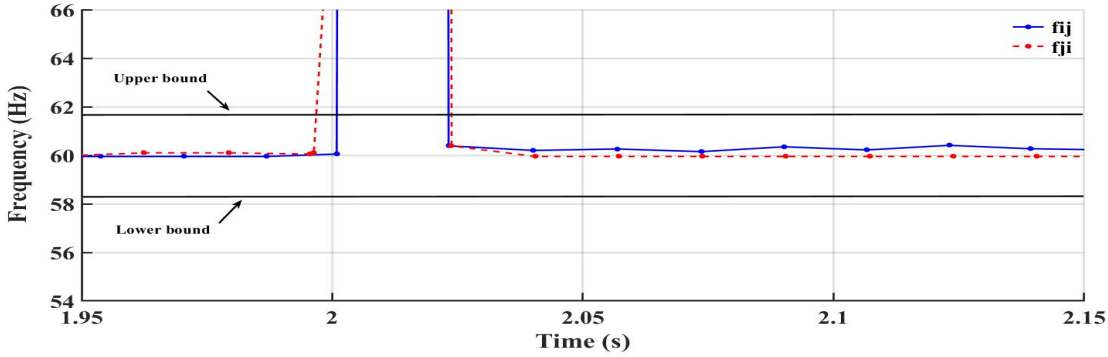

Figure 3.27: Frequency of I_{ij} and I_{ji} for an ABG fault at the beginning of line jk ($s = -30\%$).

3.5 Summary

Because of the ability of the DFIG to operate during sub- and super-synchronous conditions, the slip of the generator changes in the range of $\pm 30\%$. The change in the slip of the DFIG affects the frequency of the fault current and it deviates from the nominal frequency during the occurrence of a fault. On the other hand, the frequency of the voltage remains near the nominal frequency. Hence, the off-nominal frequency of the fault current captured by the relay at the DFIG-based WF substation leads to significant changes in the

impedance trajectory calculated by the relay, resulting in the loss of coordination between the adjacent relays.

The modified distance element type II provides reliable protection over the entire length of the transmission line connected to the DFIG-based WF with the minimum bandwidth requirement. Furthermore, the modified distance element type II can provide proper backup protection for the adjacent lines with the help of the modified distance element type I which was developed in Chapter 2.

Chapter 4

Conclusions and Future Work

4.1 Conclusions

The development of WFs is experiencing considerable growth worldwide. The large integration of WFs into the power systems will result in various challenges in the protection systems. In this dissertation, the impacts of DFIG-based WFs on the protective relaying systems have been investigated. The studies also covered fixed-speed SCIG-based WFs due to the same expression of the fault current injected by a DFIG and a fixed-speed SCIG. The studies were based on time-domain simulations of the fixed-speed SCIG- and DFIG-based WFs in the PSCAD/EMTDC environment and processing of the waveforms in the MATLAB environment. This study focused on *i*) demonstrating the negative impacts of IG-based WFs on the performance of conventional distance relays and *ii*) developing two modified relaying algorithms to overcome the identified protection challenges associated with conventional distance elements.

According to the constant flux linkage theorem, an fixed-speed SCIG can be modeled as a voltage source in series with an impedance immediately after a balanced fault. After the onset of a balanced fault, the fault current injected by the fixed-speed SCIG-based WF rises significantly. For a few cycles after the fault inception, due to the voltage drop at the terminal of the SCIG, the machine air-gap flux decreases gradually, which results in

the fast damping of dc and ac components of the fault current. Finally, the fault current reaches zero after several hundred milliseconds due to the complete demagnetization of the core of the SCIG. Reduction in the fault current leads to an increase in the impedance error calculated by the impedance relay at the SCIG-side terminal as the impedance error is inversely proportional to the fault current magnitude. The fault current reduction will be problematic when the location of the balanced fault is in zone 2 of the distance relay. In this situation, due to a large impedance error, the impedance trajectory leaves zone 2 of the distance relay before the time delay that is for the operation of the zone 2 element. The impedance trajectory may either enter zone 1 or leave the protection zones depending on the active and reactive power exchange between the SCIG and the ac grid. Assuming the impedance trajectory enters zone 1, the coordination between the distance relay at the SCIG terminal and the downstream relays will be lost, resulting in an incorrect operation of the impedance relay. Furthermore, the impedance relay at the SCIG terminal cannot provide proper backup protection for the adjacent line if the impedance trajectory leaves the relay's zones. For an unbalanced fault, the impedance trajectory will not leave zone 2 as the current magnitude does not immediately decay to zero, which will result in proper backup protection for the adjacent line. The reason is that the air-gap flux during the unbalanced fault scenario does not decrease as much as the balanced fault scenario due to the higher voltage values in the healthy phases. It should be noted that the aforementioned problem occurs for distance relays at the terminal of DFIG-based WFs when the DFIG is operating at close-to-zero slip.

The expression of the fault current injected by a DFIG-based WF is similar to that of a fixed-speed SCIG-based WF in case of the crowbar circuit activation during a balanced fault. However, the frequency of the ac component of the fault current depends on the machine slip. Since the slip of a DFIG changes in the range of $\pm 30\%$, the frequency of the fault current changes in the range of 42-78 Hz for a 60 Hz system. On the other hand, the frequency of the voltage at the relay location during a balanced fault is dictated by the ac grid and remains within a narrow margin of the nominal frequency. As a distance relay operates based on the fundamental frequency components of voltage and current, the unequal value of the voltage and current frequencies prevents the distance relay to calculate a meaningful impedance. Hence, the impedance trajectory calculated by the

distance relay will be chaotic and unreliable. This condition will be problematic when a balanced fault occurs on the adjacent line, where it is protected by zone 2 of the distance relay. In this situation, the impedance trajectory may enter zone 1, which results in loss of coordination between the distance relay at the DFIG terminal and the downstream relays. A distance relay at the terminal of a DFIG-based WF may experience the same situation as that of a balanced fault when an unbalanced fault occurs close to the DFIG (in zone 1). After the onset of an unbalanced fault, the magnitude of the decaying ac component of the fault current at the rotor frequency will be considerable. In this situation, the decaying ac component at the rotor frequency will affect the fault current frequency; therefore, the impedance trajectory calculated by the distance relay at the DFIG terminal may experience an unreliable behavior. However, this will not have a drastic effect on the performance of distance relays as the impedance trajectory enters zone 1 of the relay and leads to the instantaneous operation of the relay. Unbalanced faults in zone 2 of the relay do not result in large current components with the rotor frequency and therefore, do not affect the operation of conventional distance relays.

To overcome the protection challenge associated with the operation of distance relays at the terminals of fixed-speed SCIG or DFIG-based WFs in case of a balanced fault in zone 2, a new relaying algorithm requiring only local measurements called modified distance element type I was presented in Chapter 2. To detect a fault, the modified distance element type I uses the impedance measured at the relay location together with the phase fault current waveform injected by the SCIG or DFIG. After the onset of a balanced fault, the apparent impedance measured by the relay is used to differentiate between balanced faults in zones 1 and 2 of the relay. Then, the damping characteristics of the fault current injected by the fixed-speed SCIG- or DFIG-based WF are used to provide reliable coordination between the distance relay at the SCIG or DFIG terminal and the downstream relays.

To protect the transmission lines connected to a DFIG-based WF, a new relaying algorithm, with minimum bandwidth requirements, called modified distance element type II was presented in Chapter 3. The modified distance element type II uses the time-frequency curves, extracted from the fault currents measured at the distance relays at the two ends of the transmission line connected to a DFIG-based WF, to distinguish between internal and external faults. The developed algorithm provides reliable operation

for different types of short-circuit faults.

4.2 Future Work

In this dissertation, a number of protection challenges associated with the integration of IG-based WFs into the power system are investigated. The remaining protection challenges in systems with integrated WFs should be explored in future researches. The future research directions may include

- The effects of converter-interfaced synchronous generator (CISG)-based WFs on distance relays,
- Evaluating the impacts of WFs on the protection relays in distribution systems and microgrids,
- Performance evaluation of wide-area protection systems in the presence of WFs.

References

[1] B. Wu, Y. Lang, N. Zargari, and S. Kouro, *Power conversion and control of wind energy systems*. John Wiley & Sons, 2011.

[2] M. Tsili and S. Papathanassiou, "A review of grid code technical requirements for wind farms," *IET Renewable Power Generation*, vol. 3, no. 3, pp. 308–332, Sep. 2009.

[3] R. Burrett *et al.*, "Renewable energy policy network for the 21st century," 2009.

[4] T. Burton, N. Jenkins, D. Sharpe, and E. Bossanyi, *Wind energy handbook*. John Wiley & Sons, 2011.

[5] E. Muljadi, C. P. Butterfield, B. Parsons, and A. Ellis, "Effect of variable speed wind turbine generator on stability of a weak grid," *IEEE Trans. Energy Conv.*, vol. 22, no. 1, pp. 29–36, Feb. 2007.

[6] T. Ackermann, *Wind power in power systems*. John Wiley & Sons, 2005.

[7] M. B. Salles, K. Hameyer, J. R. Cardoso, A. Grilo, C. Rahmann *et al.*, "Crowbar system in doubly fed induction wind generators," *Energies*, vol. 3, no. 4, pp. 738–753, Apr. 2010.

[8] A. Junyent-Ferré, O. Gomis-Bellmunt, A. Sumper, M. Sala, and M. Mata, "Modeling and control of the doubly fed induction generator wind turbine," *Simulation Modelling Practice and Theory*, vol. 18, no. 9, pp. 1365–1381, Oct. 2010.

[9] J. P. Da Costa, H. Pinheiro, T. Degner, and G. Arnold, "Robust controller for dfigs of grid-connected wind turbines," *IEEE trans. ind. electron.*, vol. 58, no. 9, pp. 4023–4038, Dec. 2010.

[10] J. Liang, W. Qiao, and R. G. Harley, "Feed-forward transient current control for low-voltage ride-through enhancement of dfig wind turbines," *ieee trans. energy conv.*, vol. 25, no. 3, pp. 836–843, Aug. 2010.

[11] "Type 3 wind turbine generators (wtg) (for pscad v4.6)." [Online]. Available: https://hvdc.ca/knowledge-base/read,article/496/type-3-wind-turbine-generators-wtg-for-pscad-v4-6/v:

[12] V. Akhmatov, "Variable-speed wind turbines with doubly-fed induction generators part ii: Power system stability," *Wind Engineering*, vol. 26, no. 3, pp. 171–188, May 2002.

[13] R. Pearmine, Y. Song, and A. Chebbo, "Influence of wind turbine behaviour on the primary frequency control of the british transmission grid," *IET Renewable Power Gen.*, vol. 1, no. 2, pp. 142–150, Jun. 2007.

[14] A. Hooshyar, M. A. Azzouz, and E. F. El-Saadany, "Distance protection of lines emanating from full-scale converter-interfaced renewable energy power plants—part i: Problem statement," *IEEE Trans. Power Del.*, vol. 30, no. 4, pp. 1770–1780, Nov. 2014.

[15] A. Ghorbani, H. Mehrjerdi, and N. A. Al-Emadi, "Distance-differential protection of transmission lines connected to wind farms," *International Journal of Electrical Power & Energy Systems*, vol. 89, pp. 11–18, Jul. 2017.

[16] V. P. Mahadanaarachchi and R. Ramakuma, "Impact of distributed generation on distance protection performance-a review," in *2008 IEEE Power and Energy Society General Meeting-Conversion and Delivery of Electrical Energy in the 21st Century*. IEEE, Jul. 2008, pp. 1–7.

[17] R. Jain, B. K. Johnson, and H. L. Hess, "Performance of line protection and supervisory elements for doubly fed wind turbines," in *2015 IEEE Power & Energy Society General Meeting*. IEEE, Jul. 2015, pp. 1–5.

[18] A. Hooshyar, M. A. Azzouz, and E. F. El-Saadany, "Distance protection of lines connected to induction generator-based wind farms during balanced faults," *IEEE Trans. Sustain. Energy*, vol. 5, no. 4, pp. 1193–1203, Oct. 2014.

[19] G. M. Zubiri, S. L. Barba, I. D. L. F. DEL CASTILLO, and M. O. DEL PINO, "Impact on the power system protection of high penetration of wind farms technology," *CIGRE 2010*, vol. 5, no. 204, 2010.

[20] A. Pradhan and G. Joos, "Adaptive distance relay setting for lines connecting wind farms," *IEEE Trans. Energy Conv.*, vol. 22, no. 1, pp. 206–213, Feb. 2007.

[21] R. Dubey, S. R. Samantaray, and B. K. Panigrahi, "Adaptive distance protection scheme for shunt-facts compensated line connecting wind farm," *IET Generation, Transmission & Distribution*, vol. 10, no. 1, pp. 247–256, Jan. 2016.

[22] W. A. Qureshi and N.-K. C. Nair, *Wind farm protection.* Springer, 2014.

[23] F. Sulla, J. Svensson, and O. Samuelsson, "Symmetrical and unsymmetrical short-circuit current of squirrel-cage and doubly-fed induction generators," *Electric Power Systems Research*, vol. 81, no. 7, pp. 1610–1618, Jul. 2011.

[24] R. Dubey *et al.*, "Simultaneous impact of unified power flow controller and off-shore wind penetration on distance relay characteristics," *IET Generation, Transmission & Distribution*, vol. 8, no. 11, pp. 1869–1880, May 2014.

[25] K. Elkington *et al.*, "Connection of wind farms to weak ac networks," 2016.

[26] V. Cook, *Analysis of distance protection.* Research Studies Press, 1985.

[27] P. K. Dash, A. K. Pradhan, G. Panda, and A. C. Liew, "Adaptive relay setting for flexible ac transmission systems (facts)," *IEEE Trans. Power Del.*, vol. 15, no. 1, pp. 38–43, Jan. 2000.

[28] N. D. Tleis, *Power Systems Modelling and Fault Analysis.* Oxford, U.K.: Newnes, 2008.

[29] C. B. Cooper, D. M. MacLean, and K. G. Williams, "Application of test results to the calculation of short-circuit levels in large industrial systems with concentrated induction-motor loads," *Proceedings of the Institution of Electrical Engineers*, vol. 116, no. 11, pp. 1900–1906, Nov. 1969.

[30] R. E. Doherty and C. A. Nickle, "Three-phase short circuit synchronous machines-v," *Transactions of the American Institute of Electrical Engineers*, vol. 49, no. 2, pp. 700–714, 1930.

[31] X. Chen, A. Flechsig, C. Pang, and L. Zhuang, "Digital modeling of an induction generator," *International Conference on Advances in Power System Control, Operation and Management, APSCOM-91*, pp. 720–726, 1991.

[32] S. H. Horowitz and A. G. Phadke, *Power system relaying*. John Wiley & Sons, 2008, vol. 22.

[33] A. Pradhan, A. Routray, and S. Mohanty, "A moving sum approach for fault detection of power systems," *Electric Power Components and Systems*, vol. 34, no. 4, pp. 385–399, Apr. 2006.

[34] R. Cardenas, R. Pena, S. Alepuz, and G. Asher, "Overview of control systems for the operation of dfigs in wind energy applications," *IEEE Trans. Ind. Electron.*, vol. 60, no. 7, pp. 2776–2798, Jan. 2013.

[35] Q. Tu, Y. Li, M. Huang, S. Jiao, B. Du, Y. Zheng, and Y. Li, "Short-circuit sequence network model of dfig with different slips," in *2018 IEEE Power & Energy Society General Meeting (PESGM)*. IEEE, Aug. 2018, pp. 1–5.